Lutetium Ion Spectroscopy

Arifin

An academic exercise presented in partial fulfillment for the degree of
Bachelor of Science with Honours in Physics

Supervisor: Assoc. Prof. Murray D. BARRETT

Department of Physics

NATIONAL UNIVERSITY OF SINGAPORE

April 2014

Acknowledgements

Deepest gratitude to everyone in the microtraps group without whom this project would not be possible. It was truly an enjoyable and enriching experience I had through the ups and downs of this project.

I take this opportunity to specifically thank my supervisor Murray for his invaluable guidances and instructions throughout this project from the beginning until the very end. It was a true priviledge for me to work with him in this project.

At this juncture I would also like to thank Radu, El Nur, Kyle and Markus for their constant support along the project, both technical and moral.

Abstract

Lutetium ion (Lu II) was recently considered as a promising candidate for high-precision single-ion based atomic clock. Lu II energy levels are structured in such a way that it possesses at least three extremely narrow clock transition candidates (848 nm, 708 nm and 4.2 μm) and a relatively narrow linewidth cyclic transition that is useful for Doppler cooling and state detection purposes. In this project, we performed optogalvanic spectroscopy and Laser Induced Fluorescence (LIF)spectroscopy to gain more precision on the wavelengths required to address the relevant levels, namely 350 nm, 646 nm, 622 nm and 451 nm (ionization). Having these wavelengths measured and the required laser systems assembled, we successfully pumped the ion from the ground state to the metastable $^3D_1$ level using the 350 nm laser, drove the cyclic transition between this metastable level and the $^3P_0$ level using the 646 nm laser, and observed the resulting fluorescence. Utilizing the 646 nm fluorescence, the lifetime of forbidden decay channels from $^3P_0$ level to $^1S_0$ or $^3D_1$ was characterized. Due to some statistical complications bound to the detection method, a generalized detection model was used to analyze the data and produced an unbiased measurement of the lifetime.

Contents

Chapter 1

Introduction

This chapter will cover a brief introduction to the energy level structure of Lutetium ion ^{175}Lu II and highlight several interesting properties associated.

1.1 Lutetium Ion

Lutetium or *Lutecium* (old spelling), also known as *Cassiopeium* or *Cassiopium* in publications before 1950, is an element with atomic number 71 located at the end of the Lanthanide series, also considered as the first element of the 6^{th} period transition metals. The only two natural isotopes of lutetium are ^{175}Lu and ^{176}Lu. The former one is the only stable isotope, with 97.41% natural abundance and nuclear spin of $I = \frac{7}{2}$. ^{176}Lu, however, is a long-lived radioisotope with a half-life of 3.78×10^{10} years, and nuclear spin of $I = 7$. The scope of this project is limited to ^{175}Lu, which will be refered to as Lu hereon, unless specified otherwise.

As part of the group IIIB of transition metal, Lu atom (Lu I) has three valence electrons. Singly ionized, Lu II has two remaining valence electrons, similar to that of neutral Barium (Ba I). The configuration of the 70 electrons of Lu II follows the standard Madelung's rule i.e. [Xe] $4f^{14}\ 6s^2$, corresponding to the $^1S_0$ term symbol. The similarity of Lu II and Ba I is more than a mere equality in number of valence electrons, but more profoundly in terms of their energy level structures described in Figure 1.1a and 1.1b below:

Figure 1.1b shows several excited states relevant to this project. Details on each of these levels can be found in Table 1.1 below. Transition wavelengths and

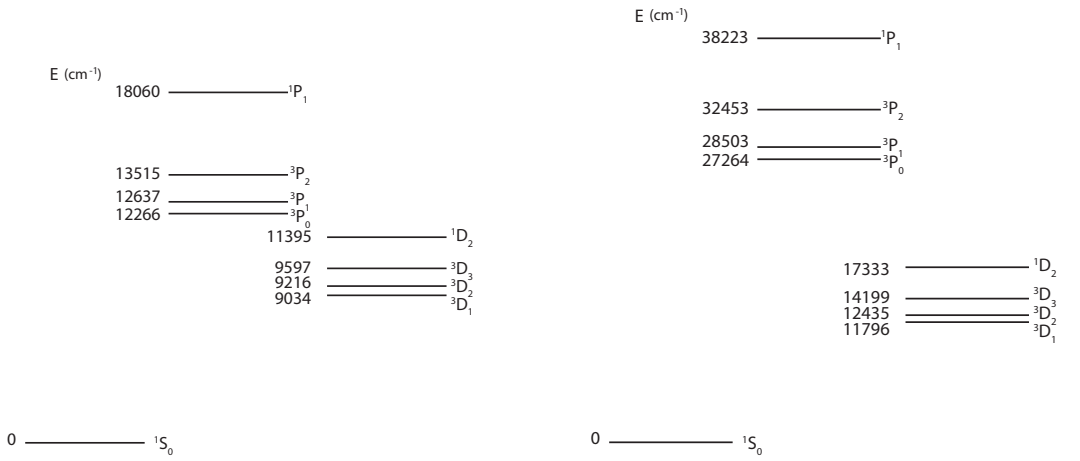

(A) Energy levels of Ba I (B) Energy levels of Lu II

FIGURE 1.1: Energy levels structure comparison between neutral Ba and Lu II

other spectroscopic data associated to these states are presented in Table 1.2 and visualized in Figure 1.2.

Configuration	Term	Energy (cm^{-1})	Lifetime (ns)	Source
$6s^2$	$^1S_0$	0	-	[1]
$6s5d$	$^3D_1$	11796.24	-	[2]
	$^3D_2$	12435.32	-	[2]
	$^3D_3$	14199.08	-	[2]
$6s6p$	$^3P^o_0$	27264.40	64.8 ± 3.2	[1]
	$^3P^o_1$	28503.16	37.4 ± 1.9	[1]
	$^3P^o_2$	32453.26	37.6 ± 1.9	[1]
	$^1P^o_0$	38223.49	2.3 ± 0.2	[1]

TABLE 1.1: Relevant energy levels of Lu II

Transition label	Upper level	Lower level	Wavelength (nm)	Branching ratio	Transition type	Rate (rad/s)
646	$^3P_0$	$^3D_1$	646.498	1±1%	Dipole	$2\pi \times 2.456$
350	$^3P_1$	$^1S_0$	350.834	0.469±7%	Spin Mixing	$2\pi \times 1.989$
598		$^3D_1$	598.554	0.160±7%	Dipole	$2\pi \times 0.681$
622		$^3D_2$	622.361	0.371±7%	Dipole	$2\pi \times 2.456$

TABLE 1.2: Relevant transitions of Lu II [2][3]

One characteristic of these structures is the energy level of the low-lying D terms that fall below both the singlet and triplet states of the P levels. It is for this

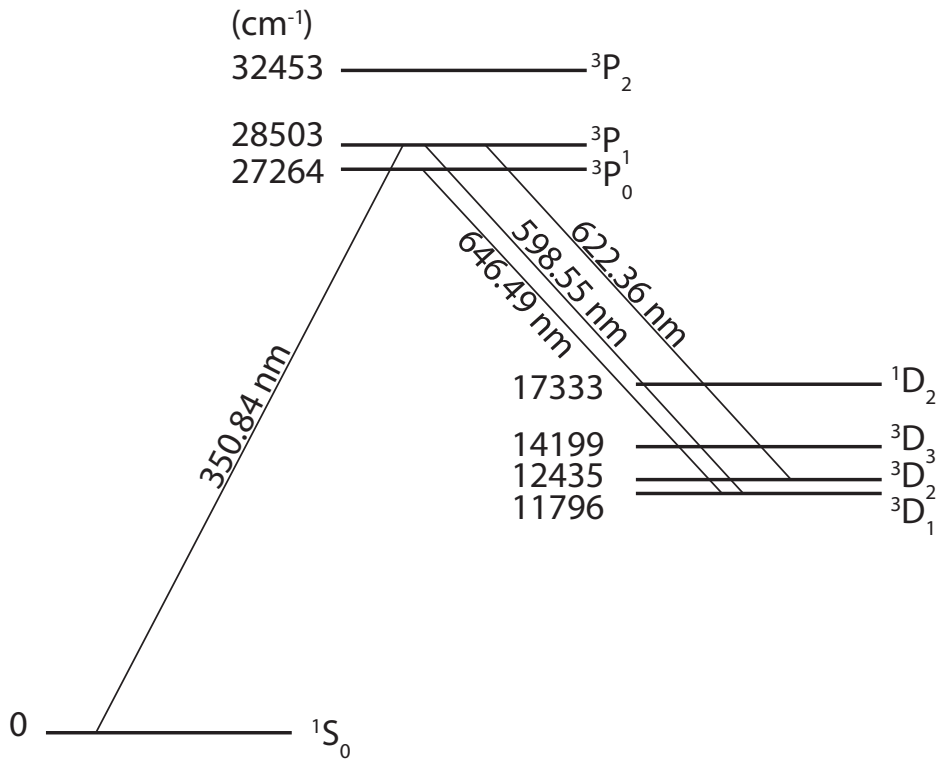

FIGURE 1.2: Diagram of relevant transitions in Lu II

reason that these two elements are considered as great candidates for ultra-high Q-factor atomic clock. This aspect will be further elaborated in Section 1.2.

For the case of neutral Barium, the phenomenon (6s5d lying below 6s6p) could be understood as a dominance of the principal quantum numbers n over orbital quantum numbers l in heavy elements. This view is supported by the fact that lighter alkaline earth atom such as Ca and Sr have their D terms and P terms interleaved [4][5]. The heavier it gets, the lower the D levels lie. This trend is somewhat reversed if we compare Lu II to lighter singly ionized atoms with two remaining valence electrons, the D terms fall even lower as the element gets lighter (Y II and Sc II) [4][6]. In the extreme case of Sc II, D terms fall even lower than S term, thus replacing its role as ground state. These observations show that Ba I and Lu II are the two elements for which the two seemingly adverse trends converge.

1.2 Project Motivation

There has been tremendous advances in the field of atomic clocks since the first realization of the ^{133}Cs clock at the National Physical Laboratory, UK in 1955 [7]. The Cs clock has enabled the redefinition of *second* in SI unit system in 1967 which is still in use to this day. A single-ion (Al II) based optical atomic clock has been reported to achieve a fractional uncertainty of 5.2×10^{-17} by Rosendband *et al.* [8] Atomic-lattice based clocks (Sr II) have also reached fractional uncertainties of 10^{16} and 10^{17} as reported by Takamoto *et al.* and Ludlow *et al.* [9][10]. The world's record for precision and stability is currently held by NIST's ytterbium atomic lattice clock at 1.6×10^{-18} instability and precision [11]. At such a high precision, applications of these clocks would go beyond GPS systems or tests of fundamental constants, but rather towards relativistic geodesy and advanced Earth-Space navigation systems.

These advancements would not have been possible without the following major breakthroughs. First, laser cooling and trapping of atoms or ions, providing isolation from environment and ultra-high suppression of Doppler effect. Second, pulse counting of optical frequencies that was recently made possible by the invention of wide-spectrum *frequency combs*, leading to higher *Q-factor* optical atomic clock. Third, development of high-finesse cavities which plays significant role in the conception of ultra-narrow linewidth laser system required in addressing individual atomic transitions and *Q-fold* power enhancement required in driving clock transitions. Fourth, precision laser spectroscopy techniques which are essential in determining wavelengths and lifetimes of various atomic transitions.

As these technologies unceasingly progress, one would naturally aim to achieve clocks with higher and higher Q-factor (a few order of magnitudes), pointing towards future candidates of atoms/ions having clock transition both in the visible-UV regime and between highly forbidden transition. Viewed from this perspective, Lu II comes up as one of the promising candidate due to the ultra-narrow clock transitions shown in Figure 1.3. The $^3D_3 - {}^1S_0$ transition at 708nm is *dipole* forbidden as $\Delta J = 3$, $\Delta S = 1$ and no parity change $\pi_i = \pi_f$; *quadrupole* forbidden since $\Delta J = 3$; and also *octupole* forbidden as $\pi_i = \pi_f$. Similarly for $^3D_1 - {}^1S_0$ transition at 848nm, it is dipole forbidden as $\Delta S = 1$ and no parity change $\pi_i = \pi_f$; quadrupole forbidden since $\Delta J = 1$; and also octupole forbidden as $\Delta J = 1$ and $\pi_i = \pi_f$. Notice also that spin-mixing mechanisms cannot occur in these transitions as there is no

nearby states of equal J to mix with. Hence, the only conceivable decay mechanism from these metastable states is by hyperfine mixing. Simulations from our collaborator estimated the lifetime of these transitions to be on the order of half a year (natural linewidth $\sim 10\,\mathrm{nHz}$). Putting this into perspective, NIST's record breaking Ytterbium clock [11] is based on the 578 nm clock transition between the ground state and $^3P_0$ state whose lifetime was determined to be at most hundreds of seconds [12].

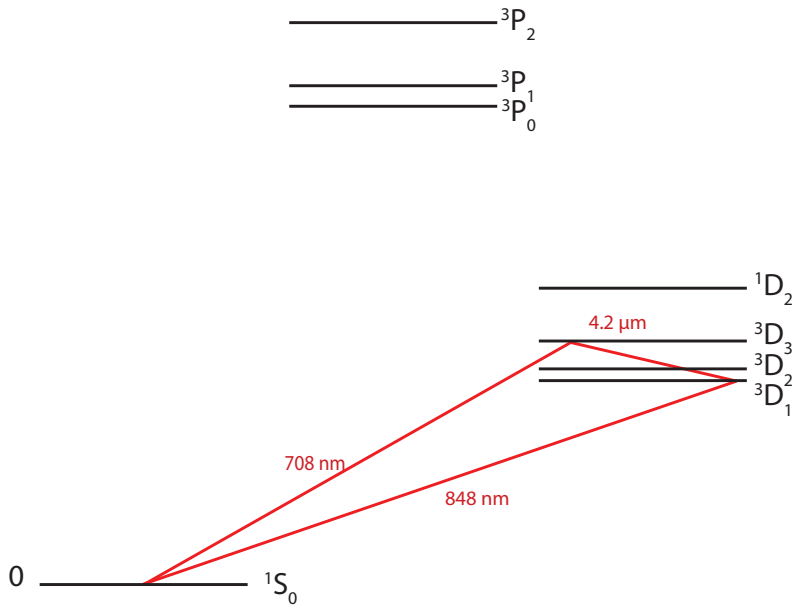

FIGURE 1.3: Highlighted in red are possible clock transitions in Lu II

Another plus side of Lu II is the fact that there are more than one accessible clock transitions in the system (ν_1 and ν_2) which can be used to create a synthetic frequency reference ν_{syn} that is immune to blackbody radiation shift using a technique proposed recently by Yudin *et al.* [13]. The realization of this method has been proposed using an optical frequency comb stabilized to ν_1 and $\nu_2$to generate a synthetic frequency ν_{syn}.

The clock transition at $4.2\,\mu$m ($^3D_1 - {}^3D_3$) could potentially be the first mid-infrared direct frequency standard with an accuracy comparable to optical or microwave atomic clock standard. Frequency standards in this spectrum have various applications in the fields of high-speed wireless communication, security, medical analysis, and material inspection.

Referring to Figure 1.2 and 1.3, one will realize that the 646nm *cyclic* transition naturally provides means of state detection and Doppler cooling. This cyclic transition is accessible by first exciting the ion from the ground state to $^3P_1$ at

350 nm, from which there is $\sim$16% chance of falling to the $^3D_1$ level (which we want) and $\sim$37% chance of falling to the $^3D_2$ level which can be pumped back to $^3P_1$ with 622 nm. It is remarkable that all these wavelengths are within the coverage of standard diode lasers (cf. Table 1.2), except for 350 nm which will require frequency doubling.

A more direct application of this project is to make use of Lu II as a cooling agent for other species of ions or even neutral atoms. As Doppler cooling performance is directly dependent on the cooling transition linewidth (cf. Section 2.4), Lu II will make a good cooling agent as the 646nm transition has a rather narrow linewidth $\Gamma \simeq 2\pi \times 2.5$ MHz (cf. Table 1.2), an order of magnitude narrower than the 493 nm cooling transition of ^{138}Ba currently used in our lab.

1.3 Project Overview

The aim of this project is to perform preliminary assessment of Lu II as a clock candidate. Our first step is to acquire more precise wavelength information of the relevant transitions through optogalvanic and Laser Induced Fluorescence (LIF) spectroscopy. Wavelength data (Table 1.2) currently available is only accurate down to a few picometers or a few GHz in terms of frequency. This is far from sufficient to perform further measurements on a single ion, especially in our case where the linewidths of interest are on the order of a few MHz.

Once the required wavelengths are known, we would attempt to prepare the ion in the metastable D states via the P levels and to drive the 646 nm cyclic transition and observe the fluorescence. The fluorescence can then be collected on a CCD camera as a means to literally *see* the ion. This part involves the trapping of Lu ion, setting up the relevant laser systems and an imaging system. The trapping of Lu ion was performed before this project and detailed in the Master's thesis [14], although it was not thoroughly confirmed if the ion trapped was indeed Lu II.

The next step is to quantify the decay rate of the $^3P_0 - {}^1S_0$ and $^3P_0 - {}^3D_2$ transitions which are forbidden under LS coupling picture through quantitative measurement of fluorescence behavior at 646 nm. This part involves the installation of a Single Photon Counting Module (SPCM) onto the imaging system and a pinhole for spatial filtering.

Chapter 2

Background Theory

This chapter will provide brief theoretical discussion on some concepts and techniques relevant to this project. Optogalvanic spectroscopy and laser Induced Fluorescence (LIF) spectroscopy techniques were used for preliminary determination of relevant atomic transitions. Subsequent measurements were done on a single ^{175}Lu II ion confined in a linear Paul trap, sympathetically cooled using ^{138}Ba ions. Basic concepts pertaining to the trapping and cooling of ions will also be addressed.

2.1 Optogalvanic Spectroscopy

This spectroscopy technique measures the effect of laser induced transitions between two atomic/molecular energy levels in gas discharge to the current consumption I of the discharge lamp. The closer the laser to the resonance, more transitions are induced which giving rise to higher signal.

Let $E_i \rightarrow E_k$ be the transition of interest, where the two levels have different ionization probabilities $P(E_i)$ and $P(E_k)$, and assume the ionization process is directly dependent on the electron bombardment $\sim I$, it follows that if a laser introduces a change in the steady-state populations of E_i and E_k by Δ, the resulting change in current consumption would then be $\delta I = \kappa[(n_k + \Delta)P(E_k) - (n_i - \Delta)P(E_i)]$, κ being the proportionality constant. The current signal can then be converted into voltage V by a sense resistor. This signal will give an indication on how much population change Δ has taken place which is directly proportional

to the detuning of the laser frequency with respect to the atomic transition of interest.

The signal, however is typically weak and requires lock-in detection, a technique used to measure very small signals obscured by noise. The key concept here is phase-sensitive detection whereby the signal is modulated at a given frequency ($V_{sig}\sin(\omega t+\theta_{sig})$) that is far from where the noise spectrum is concentrated. The modulated signal is then captured by phase sensitive detector (PSD), amplified, and multiplied by the reference frequency ($V_{ref}\sin(\omega t+\theta_{ref})$). The resulting signal V_{out} is the following:

$$\begin{aligned} V_{out} &= V_{sig}V_{ref}\sin(\omega t+\theta_{sig})\sin(\omega t+\theta_{ref}) \\ &= \frac{1}{2}V_{sig}V_{ref}\cos(\theta_{sig}-\theta_{ref}) - \frac{1}{2}V_{sig}V_{ref}\cos(2\omega t+\theta_{sig}+\theta_{ref}) \end{aligned} \tag{2.1}$$

Upon filtering with a low-pass filter, we obtain a clean DC signal (the first term). Any noise components which are not close to ω_{ref} will be highly attenuated as they will not result in DC signal on the output.

Optogalvanic spectroscopy is known for its remarkable sensitivity and good signal to noise ratio. Doppler-free saturated absorption spectroscopy can be performed in conjunction with this method using a *see-through* hollow cathode lamp[15]. Additionally, an optical resonator may be used to enhance laser intensity. The performance of this method declines as the wavelength range goes towards the UV regime where the cathode starts experiencing photoelectric effect. More elaborate treatment of this method can be found in [16], details on the actual experimental setup, diagram and parameters are presented in Section 3.1.

2.2 Laser Induced Fluorescence Spectroscopy

Contrary to the previous technique, LIF signal is acquired from re-emission of light (via spontaneous emission) that follows laser induced excitations from E_i to E_k. As such, re-emitted photons are of several different wavelengths corresponding to each of the allowed atomic/molecular transition from the excited state E_k to the lower levels. One could then immediately infer the differences in energy levels and transition probabilities of the terminating levels from the wavelength and relative amplitude differences of the fluorescence lines respectively. The absolute

amplitudes of the signal would then be proportional to the excitation probability of $E_i \rightarrow E_k$ which in turn, is proportional to the detuning of laser's frequency to the actual atomic transition frequency.

As there is no preferred direction in spontaneous emission, the fluorescence radiates in all direction, this poses a technical challenge to obtaining high collection efficiency. In most cases, a high-efficiency photodiode or a photomultiplier tube (PMT) is required to capture the fluorescence. One foreseeable challenge in performing LIF spectroscopy on gas discharge arises from the fact that the discharge lamp itself is already emitting light in all spectral lines of the elements in the plasma without laser excitation. This will negatively influence the signal to noise ratio especially when laser power is a constraint. More elaborate treatment of this method can be found in [16], details on the actual experimental setup, diagram and parameters are presented in Section 3.2.

2.3 Linear Paul Trap

Unlike neutral atoms, ions can be trapped using clever arrangement of electric fields and/or magnetic fields thanks to their net charge. There are in general two families of ion traps: Penning trap that makes use of static electric and magnetic fields, and Paul rf trap that uses a combination of static and oscillating electric fields. Figure 2.1 describe the typical design of a linear Paul trap where an oscillating electric field $V_0 \cos \Omega t$ is applied to the electrodes labeled 2 and 4 (cf. Figure 2.1b) whereas the adjacent electrodes (1 and 3) are grounded.

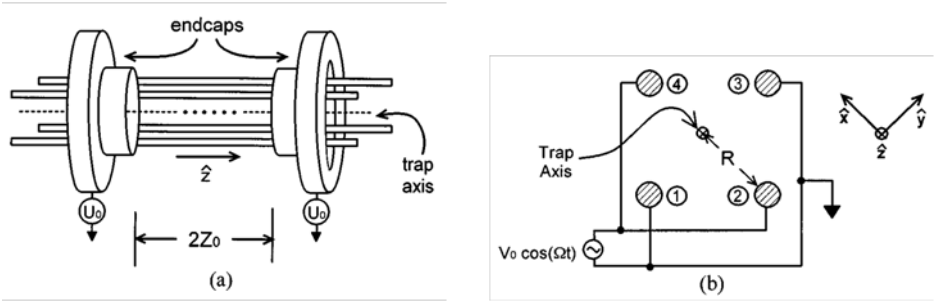

(A) Side view (B) Cross-section view

FIGURE 2.1: Linear Paul trap diagram. [17]

Taking the above-mentioned potentials as boundary conditions to the Laplace equation $\nabla^2 \Phi = 0$ [18], the approximate potential near the z-axis of the trap is

the following:

$$\Phi_r \simeq \frac{V_0 \cos \Omega t}{2}\left(1 + \frac{x^2 - y^2}{R^2}\right) \tag{2.2}$$

Notice that when the value of $\cos(\Omega t)$ is positive, Φ_r forms harmonic confinement in x direction and anti-harmonic in y direction. The inverse is true when $\cos(\Omega t)$ is negative. One could then picture this potential oscillating between these two states at a frequency of $\Omega/2\pi$, alternately providing confinement in both x and y direction. With proper choice of Ω, the ion is effectively trapped by a harmonic potential or *pseudopotential* $\Phi_p = \frac{q}{2} m\omega_r^2(x^2 + y^2)$[19]. The expression for ω_r and its physical meaning will be further explained in this section.

Having static voltage U_0 applied to both endcaps (cf. Figure 2.1a), the resulting potential along the z direction near the center of the trap is as follows:

$$\Phi_z = \frac{m}{2q}\omega_z^2\left[z^2 - \frac{1}{2}(x^2 + y^2)\right], \tag{2.3}$$

where $\omega_z^2 = \dfrac{2\kappa q U_0}{m Z_0^2}$ and κ is a geometric factor. It is evident that this potential provides harmonic confinement along z axis. Applying Newton's second law to a particle of mass m and charge q, we have a set of Mathieu equations as our equation of motion [19]. A solution to these equations is known as the Floquet solution, describing trapped ions movement as follows:

$$\begin{aligned} u_i(t) \simeq A_i\Big(&\cos(\omega_i t + \phi_i)\left[1 + \frac{q_i}{2}\cos(\Omega t) + \frac{q_i^2}{32}\cos(2\Omega t)\right] \\ &+ \frac{q_i}{2}\left[a_i + \frac{1}{2}q_i^2\right]^{1/2}\sin(\omega_i t + \phi_i)\sin(\Omega t)\Big), \end{aligned} \tag{2.4}$$

where $i \in \{x, y\}$, $a_x = a_y = \dfrac{1}{\Omega^2}\dfrac{kqU_0}{mZ_0^2}$, $q_x = -q_y = \dfrac{2}{\Omega}\dfrac{qV_0}{mR^2}$, and A_i depends on the initial position. The above expression is an approximation to first order in a_i and second order in q_i. The dominating term is that of a simple harmonic motion with frequency ω_i, often referred to as *secular* motion. Higher order terms that oscillate at much higher frequencies Ω and 2Ω result from the AC driving field and are referred to as *micromotion*.

The amplitude of secular motion A_i can be minimized by laser cooling[20] down to the Doppler cooling limit. As the amplitude of micromotion is directly related to that of the secular motion (cf. eqn 2.4), laser cooling will also suppress

the micromotion. This is not necessarily true however if the trap is not ideal i.e. when there are stray electric fields or phase difference between electrodes 2 and 4, in which case additional micromotion terms emerge [17] with amplitudes independent of A_i. In consequence, laser cooling will no longer be able to suppress this motion as it is purely driven. Also, the minimum of the pseudopotential is shifted and no longer coincides with that of Φ_z. This type of micromotion is called *excess micromotion* which can be compensated by applying appropriate bias field to displace the trap.

Linear crystal configurations of trapped ions can be achieved when $\omega_i \gg \omega_z$. The critical ratio has been estimated analytically to be $(\omega_i/\omega_z)_c \simeq 0.73L^{0.86}$ [21]. It is also practical to break the radial degeneracy of the trap ($\omega_x \neq \omega_y$) by applying DC bias fields on the ideally grounded electrodes (1 and 3). This is done to properly define trap's x and y basis, thus ensuring laser cooling is effective in all three translational degree of freedom (cf. Section 2.4). The values of ω_x, ω_y and ω_z can be determined experimentally by observing resonance behavior when the appropriate RF frequency is applied to the electrodes or endcaps.

In our experiment, the value of ω_z is used to deduce the mass of the ions trapped as this quantity is dependent on charge to mass ratio, i.e.

$$\frac{\nu_1}{\nu_2} = \frac{\omega_{z1}}{\omega_{z2}} = \left(\frac{q_1}{m_1}\frac{m_2}{q_2}\right)^{1/2} \tag{2.5}$$

The value of ω_z can also be used to calculate the distance between ions in a linear configuration as the separation between ions is given by $s_2 = 2^{1/3}s$ for two ions, and $s_3 = (5/4)^{1/3}s$ for three ions, where $s = (q^2/4\pi\epsilon_0 m\omega_z^2)^{1/3}$. These expressions can be easily derived from the force balance equation along z-axis.

2.4 Doppler Cooling

As discussed in the previous section, laser cooling is required to suppress the secular motion of trapped ions so that a stable crystal of ions can be formed. As the name suggests, this technique is based on the fact that ions moving against the direction of the beam perceive the incoming laser to be blue-detuned. The greater the ions' velocity, the more blue-shifted the laser frequencies. It is then possible to deliver a counterforce to these high velocity ions without affecting the slow ones

by appropriately red-detuning the incoming laser frequency ω with respect to the ion's transition frequency ω_0, provided that the ion does have an closed two-level system which can be continuously driven (*cyclic*).

From a semi-classical perspective, accounting for spontaneous emission, the force experienced by an ion due to a pair of counter-propagating laser beams along the beam's axis is[22]:

$$\vec{F} = \langle \vec{F}_{abs} \rangle + \delta \vec{F}_{abs} + \langle \vec{F}_{em} \rangle + \delta \vec{F}_{em} \tag{2.6}$$

The average force due to absorption from the two beams is $\langle \vec{F}_{abs} \rangle$ from which damping behavior can be seen in the following expression:

$$\begin{aligned} \langle F_{abs} \rangle &= F_{scatt}(\Delta - kv) - F_{scatt}(\Delta + kv) \\ &\simeq \left[F_{scatt}(\Delta) - kv \frac{\partial F_{scatt}}{\partial \omega} \right] - \left[F_{scatt}(\Delta) + kv \frac{\partial F_{scatt}}{\partial \omega} \right] \\ &\simeq -\alpha v, \end{aligned} \tag{2.7}$$

where $\Delta = (\omega - \omega_0)$ is the laser's detuning and $\alpha = 4\hbar k^2 \dfrac{\bar{I}\,\overline{\Delta}}{(1+\overline{\Delta}^2)^2}$ is the damping coefficient with $\overline{\Delta} \equiv 2\Delta/\Gamma$ and $\bar{I} \equiv I/I_{sat}$, I_{sat} being the saturation intensity.

The term $\delta \vec{F}_{abs}$ in Equation 2.6 accounts for the variation in the number of photons absorbed in a given period t. The fluctuation term $\delta \vec{F}_{em}$ results from the fact that spontaneous emission process emits photons at random directions. These fluctuations impose a limit to this technique, known as the Doppler temperature $k_B T_D = \dfrac{\hbar\Gamma}{2}$, achieved when $\Delta = \Gamma/2$. The recoil frequency associated to the damping process alone is $\omega_{rec} = \dfrac{\hbar k^2}{2M}$.

The twist to this canonical picture for the case of trapped ions is that a single laser beam is sufficient as long as the laser beam has a nonzero projection to all principles axes of the trap $(\omega_x, \omega_y, \omega_z)$. The downside to this is that the Doppler limit might not be achievable as the $F_{scatt}(\Delta)$ term in Equation 2.7 no longer cancels. It is also important to ensure that $\omega_{rec} \ll \omega_{x,y,z}$. A full quantum mechanical treatment of a laser-cooled single ion in harmonic trap can be found in ref. [23].

2.5 Sympathetic Cooling

Despite the outstanding performance of Doppler cooling, the technique still lacks robustness in terms of trappable ion species as it primarily depends of the availability of suitable cooling transition in the energy level structure. The term sympathetic cooling encompasses all scenarios when one gas is cooled by a colder gas via elastic, inelastic, or charge exchange scattering [24], may it be between ions of different species, or an ion-atom hybrid system. Ion-ion sympathetic cooling is mainly facilitated by the strong Coulomb interaction. Under the *hard-sphere* model [25], the temperature of a species of mass M after k number of collision with a colder species of mass m is given by [26]:

$$T_M = T_m + (T_M^0 - T_m)e^{-k/\kappa}, \qquad (2.8)$$
$$\text{where} \quad \kappa = \frac{(M+m)^2}{2Mm}.$$

Sympathetic laser cooling can, in principle, be performed in either a Paul trap or a Penning trap. In a Penning trap, a larger mass ion tend to form a *doughnut* structure around the lower mass ones (centrifugal separation) due to the difference in their rotation frequency around the magnetic axis. This was first demonstrated by Larson *et al.* [26].

In a linear Paul trap, sympathetic cooling naturally occurs when ions of different species or isotope accidentally occupy one or a few sites of the ions crystal [27]. Although they do not fluoresce, their presence can be inferred visually [28]. The stability and the number of ions that can be trapped sympathetically are limited by rf heating and laser cooling power [20]. In our experiment, sympathetic cooling of lutetium is readily observed when lutetium ions enter the trap in which barium ions are already present.

Chapter 3

Experimental Setup

Details on experimental devices, arrangement and parameters are presented in this chapter for future reference.

3.1 Optogalvanic Spectroscopy

Actual configuration of the experiment is described in the following diagram:

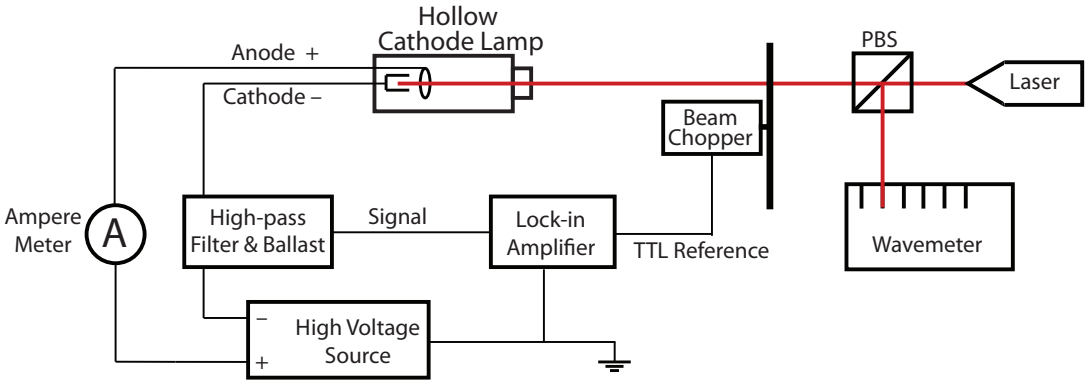

FIGURE 3.1: Diagram of Optogalvanic Spectroscopy Setup

The Hollow Cathode Lamp (HCL) used was a commercial 2″ Lutetium discharge tube from Buck Scientific with a maximum current of 12mA. An attempt to construct a see-through HCL was not successful due to plasma instability issues. A EMCO F10CT switching boost converter was used to provide high voltage ranging from 0-500V. Signal was acquired using a standard high-pass filter built-in together with ballast resistor for current regulation purpose. Components values

are provided in Figure 3.2 with a cut-off frequency tunable up to 3kHz. The lock-in amplifier in use was Stanford Research Systems SR810, taking a TTL reference directly from the beam chopper (Thorlabs), providing signal modulation at ∼500 Hz. The wavemeter used was a High Finesse WS7 with accuracy of 60 MHz when regularly calibrated.

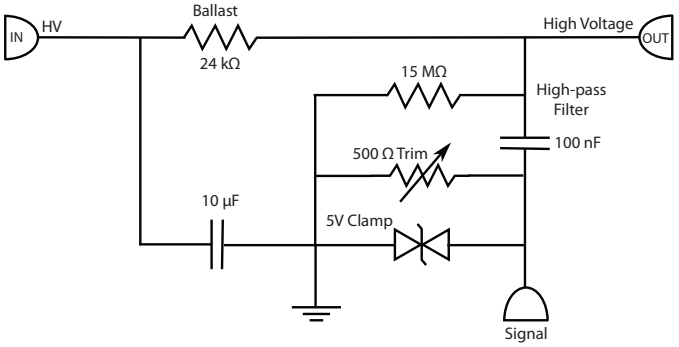

FIGURE 3.2: High-pass filter and ballast circuit

Data was recorded by manually noting down the magnitude of the voltage signal displayed on the lock-in amplifier vs wavelength value shown in the wavemeter as the laser sweep through the transition of interest. The sweeping was done by manually tuning its diffraction grating position (PZT controlled). Typical integration time was between 1s to 3 s per data point. This technique was used to measure the 646 nm transition and 451 nm ionizing transition.

3.2 LIF Spectroscopy

Laser Induced Fluorescence spectroscopy setup only require slight modification to the optogalvanic setup. The signal is captured optically by a photomultiplier tube (PMT) as decribed in Figure 3.3 below. Parameters pertaining to the lock-in detection system and data acquisition are identical to the previous method. One important point here is that the fluorescence collected by the PMT need not be the same as the wavelength of interest, as the ions might decay to more than one lower states upon excitation. It is then beneficial to chose a decay branch that has the highest rate and branching fraction by putting the appropriate filter in front of the PMT. It is also important to ensure no background light goes to the PMT. The measurement of the 350 nm transition from the ground state to the $^3P_1$ state was done by collecting the 622 nm fluorescence as the decay to the $^3D_2$ state

is more prominent. This technique was used to measure the 350 nm transition and 451 nm ionizing transition.

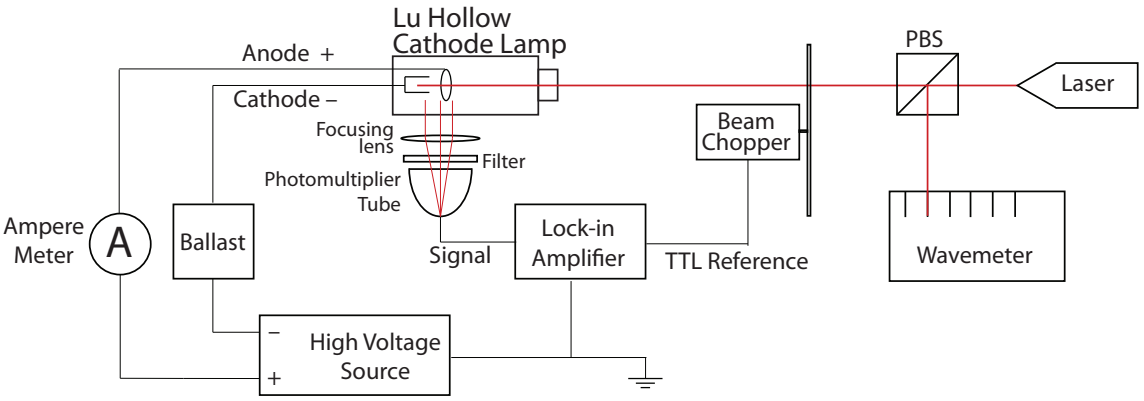

FIGURE 3.3: Diagram of LIF Spectroscopy Setup

3.3 Ion Trap

The following figure shows a diagram of the ion trap configuration at the time this report is written, viewed from the top.

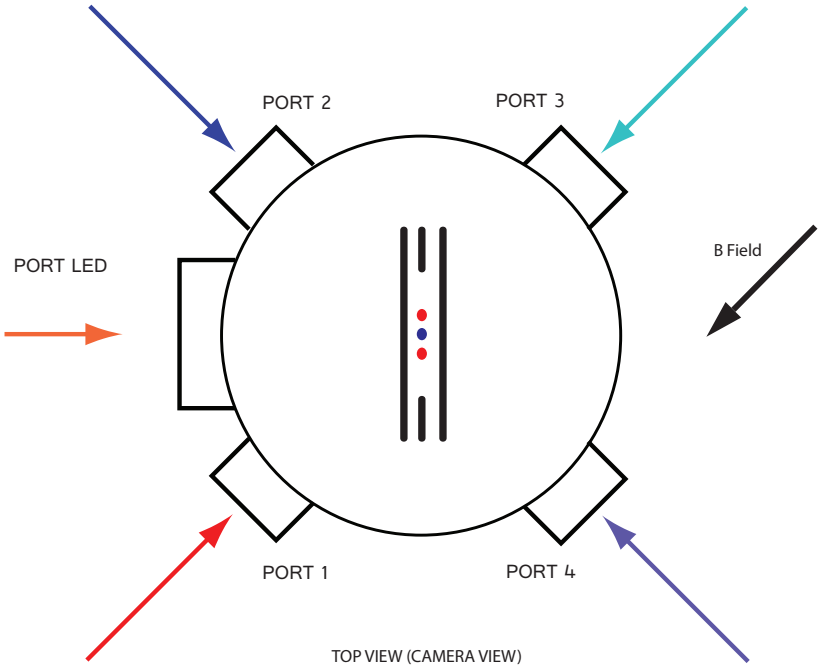

FIGURE 3.4: Trap diagram with the ports labeled

PORT 1, mounted with a RMS20X Olympus Plan Achromat for collimation and a focusing f = 150 mm achromat doublet. This port is dedicated to 646 nm

beam with a measured waist of $W_0 = 29.0 \pm 0.5\,\mu$m. Saturation power at this waist is ~ 31 nW whereas the operating power that gives the best signal to noise ratio is $3.5\,\mu$W. The incoming beam is horizontally polarized (polarization perpendicular to magnetic field) with an 0.8% extinction ratio.

PORT 2, mounted with a RMS20X Olympus Plan Achromat for collimation and a focusing f = 100 mm achromat doublet. All ionization beams come through this port i.e. 451 nm ($112\,\mu$W) for Lutetium ionization; 450 nm ($2.9\,\mu$W),791 nm ($2.4\,\mu$W) and 650 nm (2.8 mW) for Barium ionization. The power level stated here are experimentally adjusted for optimal ion loading. Focus alignment is done using 493 nm beam as an estimate.

PORT 3, mounted with a RMS20X Olympus Plan Achromat for collimation and a focusing f = 250 mm achromat doublet. Barium Doppler cooling beams (493 nm and 650 nm) come through this port. The measured waist at 493 nm is $38.5\,\mu$m and at 650 nm is $48.5\,\mu$m. The focal point of the 493 nm beam lies at the center of the trap and the 650 nm beam radius at this point is $52\,\mu$m. The saturation power for 650 nm at this radius is $\sim 0.2\,\mu$W and that of 493 nm at this waist is $\sim 0.8\,\mu$W. Normally we operate at $12\,\mu$W of 493 nm and $6.6\,\mu$W of 650 nm to obtain brighter fluorescence for easy viewing.

PORT 4, mounted with an aspheric lens A280TM-A, f = 18.4 mm for collimation and a focusing f = 150mm achromat doublet. This port is optimized for 350 nm and does not support other wavelengths as the collimation lens is not achromatic. The waist of this system measured at 493 nm is $14.5\,\mu$m with a Rayleigh range of $z_0 = 1.3$ mm. The actual waist at 350 nm was not be measured due to technical limitation (camera's sensitivity issue at 350 nm). Alignment was done by first aligning it using 493 nm beam and then further refined based on the blinking behavior of Lu fluorescence. Half a turn of the focus tuning knob corresponds to approximately 2 mm of focal displacement.

PORT LED, mounted with a telescope system consisting of two plano-convex lenses of f = 75 mm and f = 100mm, a-coat, approximately focusing most part of the light to the center of the trap. A bandpass filter FB620-10, centered at 620 nm with FWHM = 10 nm, is mounted right on the fiber output to block light at unwanted wavelengths.

As mentioned in Section 2.3, excess micromotion would result in the displacement of the pseudopotential's minima with respect to the minima of the harmonic

potential along z-axis. Thus, we can compensate this by tuning the *Bias* voltage, *Baseplate* voltage, and *Bias difference* voltage (cf. Figure 3.5) in such a way that the two minima coincide.

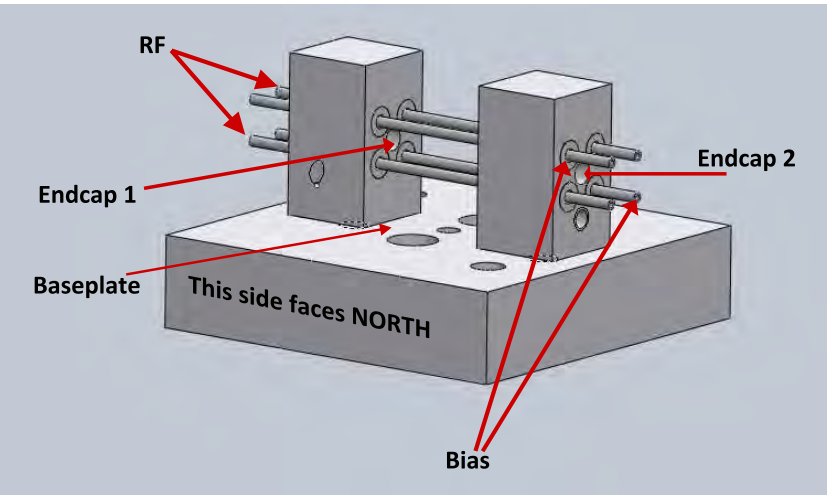

FIGURE 3.5: Trap 3D visualization with wiring labeled

Detailed description on each of these parameters can be found in Guoqing's thesis on the construction of this trap [14]. Listed below are three sets of trap parameters that minimize the excess micromotion that we know as of now. The unitless quantities in the table refer to the hash-mark label of the potentiometer ranging from 0 to 10.

Parameters	Config 1	Config 2	Config 3
Bias diff	5.12	5.27	8.585
Endcaps diff	4.99	4.99	4.95
Bias	6.08	6.54	6.15
Endcaps	3.20	6.40	8.6
Baseplate	5.5 V	7.0V - 42.0V	40.6V
^{138}Ba ω_z	$2\pi\times$ 48kHz	$2\pi\times$ 75.5kHz	$2\pi\times$ 91.1kHz
Comment	Easy for bulk loading	Better multispecies ions stability	Best stability for 2Ba and 1Lu

The baseplate voltage required to minimize micromotion increases from 28V to 41V over a period of 3 months due to charging effect of the ceramic at the baseplate. Knowing this issue, one shall not take the baseplate values quoted in the table as an absolute. At $\omega_z = 75.5\,\text{kHz}$, the separation between ions is $s_2 \simeq 24\,\mu\text{m}$ and $s_3 \simeq 19\,\mu\text{m}$ (cf. Section 2.3). These values are in accordance to visual observation through the camera (cf. Section 3.5).

3.4 Laser Systems

As the Lu ion is cooled sympathetically by Ba ions, both laser systems associated to Ba and Lu are required in the trap. This section focuses on lasers associated to Lu ionization (451 nm), ground-state pumping (350 nm), detection (646 nm) and repumping (622 nm LED). Details on lasers associated to Ba will be briefly presented at the end of this section.

The 451 nm beam, also referred to as ionization beam, excites neutral Lu (Lu I) from the ground state $^2D_{3/2}$ to $^2D^\circ_{3/2}$ (22124.76 cm^{-1}) [3] and directly ionize it from this state on (the ionization threshold is 43762.60 cm^{-1}) [29]. This method however, will not give isotope selectivity as the excitation rate is $A = 2\pi \times 3.7$ MHz. The diode used is Osram PL450B, heated to about 30° C. As this laser is only used during loading, locking mechanism is not required. During loading, laser wavelength is set to 451.98320 nm, 500 MHz away from resonance to account for the Doppler shift due to atoms' velocity as they come out of the oven. This detuning is estimated by taking the rms velocity of the atoms at oven temperature of 900 K and beam incident at 45° angle. It is observed that this laser radiation pumps Barium ion into a dark state, hence the need of keeping the 622 nm LED on during Lutetium loading as the LED spectrum spans over to the 615 nm range.

The 350 nm beam, also referred to as pumping beam ($^1S_0 - {}^3P_1$), is derived from a frequency doubled 40 mW 701 nm diode laser HL7001MG-A operating at 20° C with grating-stabilized linewidth of 300 kHz. Frequency doubling is done by a 10 mm Brewster cut BBO crystal in a bow-tie cavity configuration, producing up to 120 μW output power. This laser is locked to a temperature stabilized cavity with FWHM $\simeq 4.8$ MHz. The frequency of this laser is tunable via fine tuning of the reference cavity temperature which shall be kept around room temperature. Following the result from LIF spectroscopy (Section 4.1), the wavelength to aim for is 701.68004 ± 16 nm which correspond to the $F = 7/2$ hyperfine level of $^3P_0$.

The 646 nm beam, also referred to as detection beam, drives the cyclic transition ($^3P_0 - {}^3D_1$) by addressing the three hyperfine splittings of $^3D_1$. Transition to $F = 7/2$ occurs at 646.49149 nm, $F = 9/2$ at 8.387 GHz higher in frequency and $F = 5/2$ at 8.231 GHz lower. At the moment this is achieved using an EOSpace device that puts two sidebands at 8.231 GHz apart from the carrier, and an AOM in double pass configuration that provides the 155 MHz correction to the other

sideband. So, there are six frequencies at the output, three of which address the hyperfine levels. This system will be simplified in the future by sending in a mixture of two frequencies with $\pi/2$ phase difference into the EOSpace device which will produce four sidebands via phase modulation as follows:

$$E_0 e^{i[\omega t+\beta \sin(\omega_1 t)\cos(\omega_2 t)]} \simeq E_0 e^{i\omega t}[1 + i\beta \sin(\omega_1 t)\cos(\omega_2 t)]$$
$$= E_0 e^{i\omega t} + E_0 \frac{\beta}{4}[e^{i(\omega_1+\omega_2)t} + e^{i(\omega_1-\omega_2)t} - e^{-i(\omega_1+\omega_2)t} - e^{-i(\omega_1-\omega_2)t}]. \quad (3.1)$$

This way, we can independently address $F = 9/2$ and $F = 5/2$ states by setting $2\,\omega_2 = 8.38\,\text{GHz}$ and $2\,\omega_1 = 8.23\,\text{GHz}$. The existing AOM can then be used to switch the beam on and off.

A transfer cavity is used to lock the 646 nm laser to an 852 nm reference laser which itself is locked to $(^2S_{1/3},\ F = 4)$ to $(^2P_{3/2},\ F = 4\,\text{co}\,5)$ transition in Cesium D2 line at 852.35677 nm. The diode in use is HL6385DG heated to 39° C. Figure 3.6 shows a schematic of the entire 646 nm system.

The repump LED used is Thorlabs M625F1 with total output power of 10 mW and dominant wavelength ranging from 620 nm to 632 nm. A bandpass filter at 620 ± 2 nm is mounted at the output of the fiber. Assuming the spectral distribution is Lorentzian, the effective power at 622.361 nm $\pm$ 10 MHz is only 1.6 nW or equivalently 0.0005 W/m^2 intensity at 2 mm diameter focus, too low for adequate repumping ($I_{sat} = 8.55$ W/m^2).

The 5 Barium beams are tapped from the barium experiment (concurrently going on in the lab). Beams associated to the ionization process namely 450 nm, 791 nm and 650 nm high power are tapped directly using a 50:50 beam splitter and coupled into one fiber. Beams associated to barium cooling are tapped right from the laser source and pass through AOM devices before going to the trap. The 493 nm beam goes through AOM21 in a double pass configuration $2\times$ 220.8 MHz, 20 MHz red-detuned with respect to the beam going towards another ion trap. The 650 nm beam goes through AOM19 in a double pass configuration $2\times$ 93.4 MHz, no detuning with respect to the beam going towards another ion trap.

3.5 Imaging System and Data Acquisition

The imaging system in use is described in Figure 3.7 below: The entire system

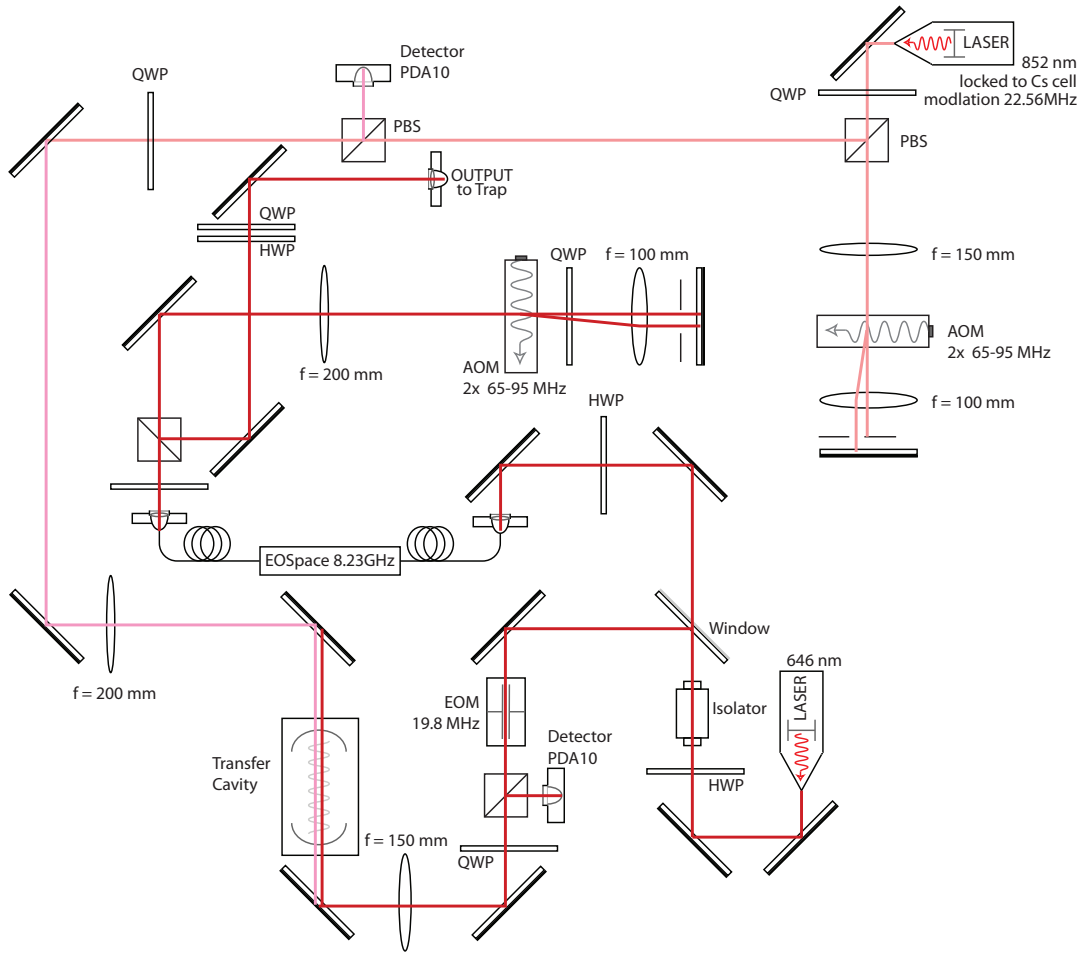

FIGURE 3.6: Schematic of the optical system to address $^3D_1$ hyperfine splittings at 646nm.

is light-tight to ensure maximal noise reduction due to external light. As such, the main noise contribution is from scattered light inside the vacuum chamber. The back focal length of the first objective is $f_b = 6.99\,\text{mm}$, placed 12.57 mm above the trap window.

Two filter slots were mounted right before the pinhole to accommodate combinations of filters to isolate different fluorescences such as 493 nm and 650 nm fluorescence of barium and 646 nm fluorescence from lutetium. Several filters we have at our disposal are Semrock LL01-647-12.5 with typical bandwidth of $647 \pm 1.25\,\text{nm}$, Semrock dual-bandpass FF01-495/640-25 with nominal bandwidths of $495 \pm 32\,\text{nm}$ and $640 \pm 20\,\text{nm}$, Semrock FF01-650/13-25 with nominal bandwidth of $650 \pm 10\,\text{nm}$ and FF01-494/20-25 with nominal bandwidth of $494 \pm 12.5\,\text{nm}$. As these achromatic lenses are not perfect, slight focal adjustment need to be done to obtain focused image at different fluorescence wavelength.

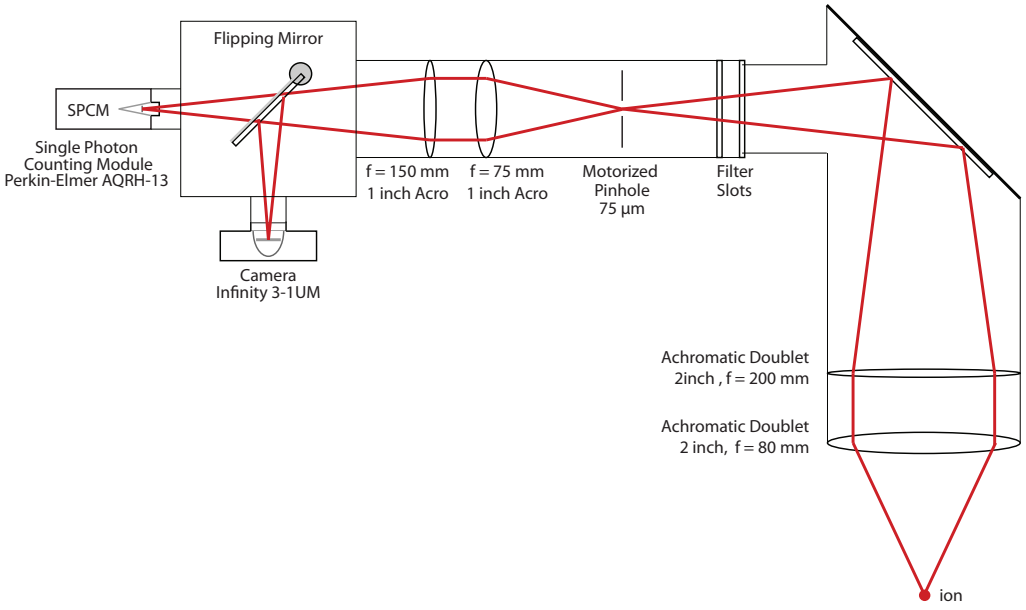

FIGURE 3.7: Imaging system diagram with selectable SPCM mode and camera mode.

The overall magnification of this system is 7.5, from which one can estimate several geometrical quantities of the ion crystal by counting the pixels of its image on the camera. The pixel size of the camera in use is $6.45\,\mu\text{m} \times 6.45\,\mu\text{m}$ and its CCD size is 1392×1040 pixels. Using this method, the separation between 2 ions (trap configuration 2) was measured to be $\simeq 22.4\,\mu\text{m}$, in agreement to theoretical calculation in Section 3.3.

Below is a sample image of Barium-Lutetium hybrid crystal at 485 ms exposure with both 650 nm filter and 495/640 nm filters on.

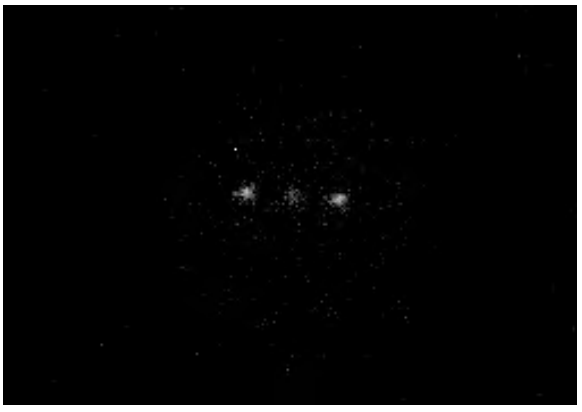

FIGURE 3.8: From left to right Barium-Lutetium-Barium at 485 ms exposure and 400 μm pinhole

The Single Photon Counting Module (SPCM) in use is Perkin-Elmer SPCM-AQRH-13 with dark count of 149 c/s. The active area of this device is circular with diameter 180 μm which at 7.5 magnification, will only capture the fluorescence of 1 ion as the end-to-end length of the 3 ions chain in Figure 3.8 is 53 pixels or $\simeq$ 342 μm. For every single photon that hits the active surface, the counting module will send out a 17 ns pulse followed by 30 ns deadtime which sets the upper limit on the photon count rate 30 MHz. The counting of these pulses is done by a 32-bit counter board NI PCI-6602 with maximum source frequency of 80 MHz without any prescaler. The count values for a given binning period (configurable) are stored in a buffer of configurable length before being reported to a Labview VI and written into file for further processing.

Chapter 4

Results and Analysis

Precise wavelength information of the transitions of interest was obtained through optogalvanic and LIF spectroscopy and is presented in Section 4.1.1 to Section 4.1.3. Setting the laser systems to these wavelengths, lutetium fluorescence at 646 nm was observed (cf. Figure 3.8), affirming mass-resonance indication that the ion species trapped was indeed Lu II. Switching off the 622 LED caused the ion to fall out of the cyclic transition into the $^3D_2$ level and stayed dark. Similarly, the ion went dark when the 350 nm laser was blocked. It was visually observed that the ion only went dark ~ 2 seconds after the beams were shut. Measurement of this lifetime is presented in Section 4.2.

4.1 Preliminary Spectroscopy

Spectroscopy of the 451 nm was done with both optogalvanic and LIF techniques yielding consistent result. Using optogalvanic spectroscopy, three peaks at 646 nm were measured, corresponding to the transitions to the three hyperfine splitting of the $^3D_1$ level. The optogalvanic technique does not work for the 350 nm transition as the work-function of Lutetium is 3.3 eV and the photon energy at 350 nm is $\sim$ 3.5 eV. The results of these measurements are presented in this section. The goodness of fit is represented by the reduced χ^2 value. The uncertainty to a parameter estimate is underestimated when $\chi^2 > 1$ and overestimated when $\chi^2 < 1$.

4.1.1 $^2D_{3/2} - {}^2D^\circ_{3/2}$ Transition at 451 nm

As mentioned in Section 3.1, the accuracy of this measurement is limited by the absolute accuracy of the wavemeter used i.e. 60 MHz or 0.04 pm at 451 nm. Figure 4.1 and Figure 4.2 show Gaussian fits of the data collected from optogalvanic and LIF spectroscopy respectively.

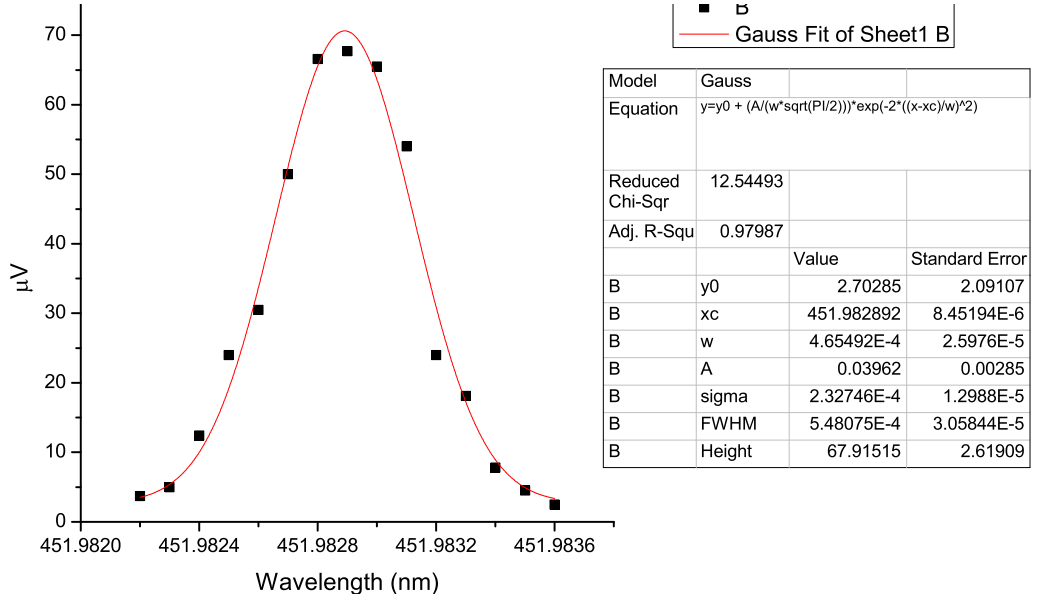

Model	Gauss		
Equation	y=y0 + (A/(w*sqrt(PI/2)))*exp(-2*((x-xc)/w)^2)		
Reduced Chi-Sqr	12.54493		
Adj. R-Squ	0.97987		
		Value	Standard Error
B	y0	2.70285	2.09107
B	xc	451.982892	8.45194E-6
B	w	4.65492E-4	2.5976E-5
B	A	0.03962	0.00285
B	sigma	2.32746E-4	1.2988E-5
B	FWHM	5.48075E-4	3.05844E-5
B	Height	67.91515	2.61909

FIGURE 4.1: Gaussian Fit of the optogalvanic measurement data of the 451 nm transition

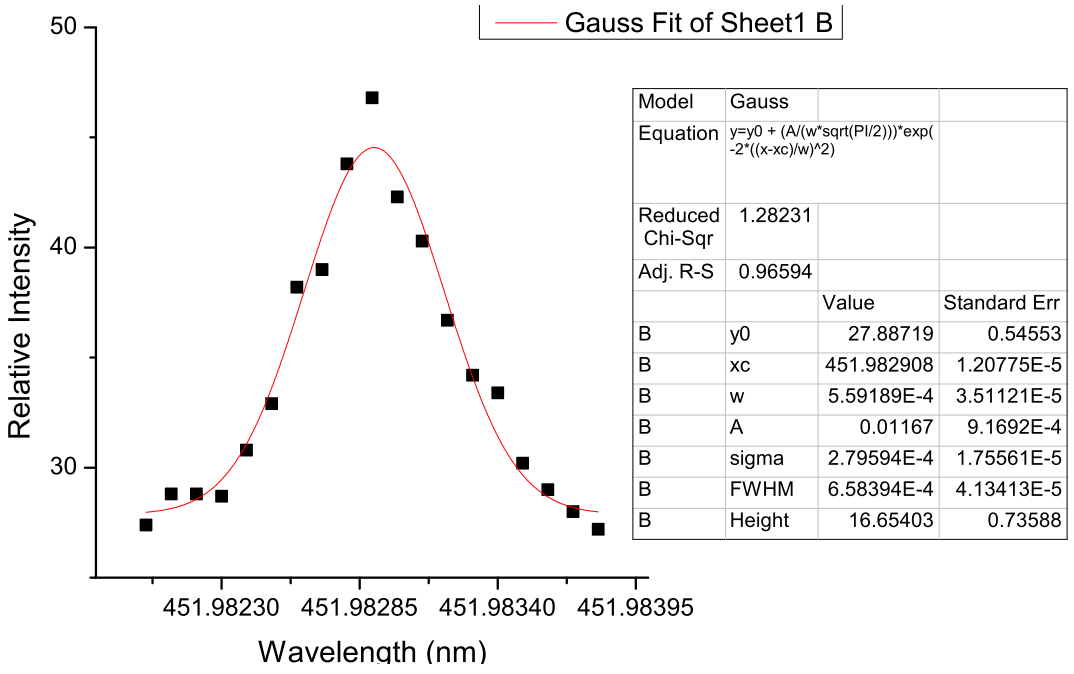

Model	Gauss		
Equation	y=y0 + (A/(w*sqrt(PI/2)))*exp(-2*((x-xc)/w)^2)		
Reduced Chi-Sqr	1.28231		
Adj. R-S	0.96594		
		Value	Standard Err
B	y0	27.88719	0.54553
B	xc	451.982908	1.20775E-5
B	w	5.59189E-4	3.51121E-5
B	A	0.01167	9.1692E-4
B	sigma	2.79594E-4	1.75561E-5
B	FWHM	6.58394E-4	4.13413E-5
B	Height	16.65403	0.73588

FIGURE 4.2: Gaussian Fit of the LIF measurement data of the 451 nm transition

The results from the two measurements differ by 0.01 pm, which is not surprising as the wavemeter accuracy is only down to 0.04 pm. As the uncertainty values from the fit is less than 0.04 pm, the value we are quoting as standard error here is that of the wavemeter. Thus, the measured wavelength is 451.98290 ± 0.00004 nm.

4.1.2 $^3P_0 - {}^3D_1$ Transition at 646 nm

The absolute accuracy of the wavemeter is 60 MHz or 0.08 pm at 646 nm. Figure 4.3, Figure 4.4, and Figure 4.5 show Gaussian fits of optogalvanic spectroscopy data corresponding to the $^3P_0$ to $(^3D_1, F = 5/2)$, $(^3D_1, F = 7/2)$, and $(^3D_1, F = 9/2)$ transitions respectively.

The results of these measurements are quoted as follows:

$$\begin{aligned} F = 5/2 &\rightarrow \lambda = 646.47981 \pm 0.00008\,\text{nm},\ \Delta\nu = +8.39 \pm 0.06\,\text{GHz} \\ F = 7/2 &\rightarrow \lambda = 646.49149 \pm 0.00008\,\text{nm},\ \Delta\nu = 0\,\text{GHz} \\ F = 9/2 &\rightarrow \lambda = 646.50296 \pm 0.00008\,\text{nm},\ \Delta\nu = -8.23 \pm 0.06\,\text{GHz} \end{aligned}$$

The $\Delta\nu$ values quoted above are the hyperfine separations with respect to the $F = 7/2$ hyperfine level. The magnetic hyperfine constant A and electric quadrupole constant B can then be inferred given that the hyperfine splittings follows the following formula:

$$E_{hfs} = A\frac{K}{2} + B\frac{\frac{3}{4}K(K+1) - I(I+1)J(J+1)}{2I(2I-1)J(2J-1)}, \tag{4.1}$$

where $K = F(F+1) - J(J+1) - I(I+1)$ [30]. Quoting in cm^{-1}, the measured coefficients are $A = -0.068 \pm 0.003\,\text{cm}^{-1}$ and $B = +0.033 \pm 0.003\,\text{cm}^{-1}$, which are in very good agreement to those reported by Hartogg *et al.* [30].

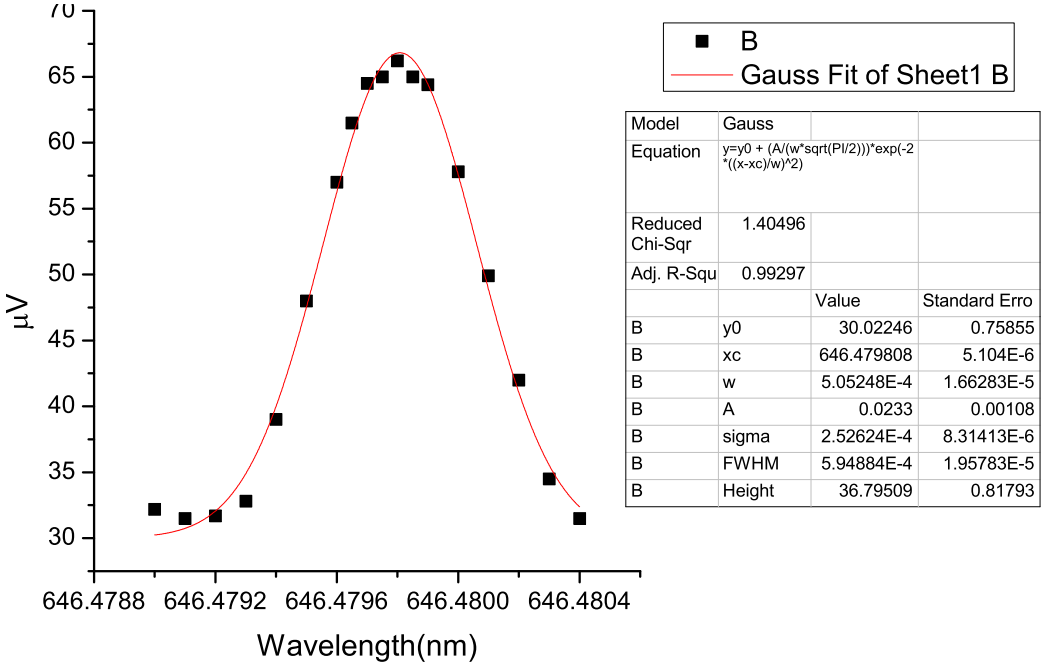

Model	Gauss		
Equation	y=y0 + (A/(w*sqrt(PI/2)))*exp(-2*((x-xc)/w)^2)		
Reduced Chi-Sqr	1.40496		
Adj. R-Squ	0.99297		
		Value	Standard Erro
B	y0	30.02246	0.75855
B	xc	646.479808	5.104E-6
B	w	5.05248E-4	1.66283E-5
B	A	0.0233	0.00108
B	sigma	2.52624E-4	8.31413E-6
B	FWHM	5.94884E-4	1.95783E-5
B	Height	36.79509	0.81793

FIGURE 4.3: Gaussian Fit of the optogalvanic measurement data of the 646 nm, $F = 5/2$ transition

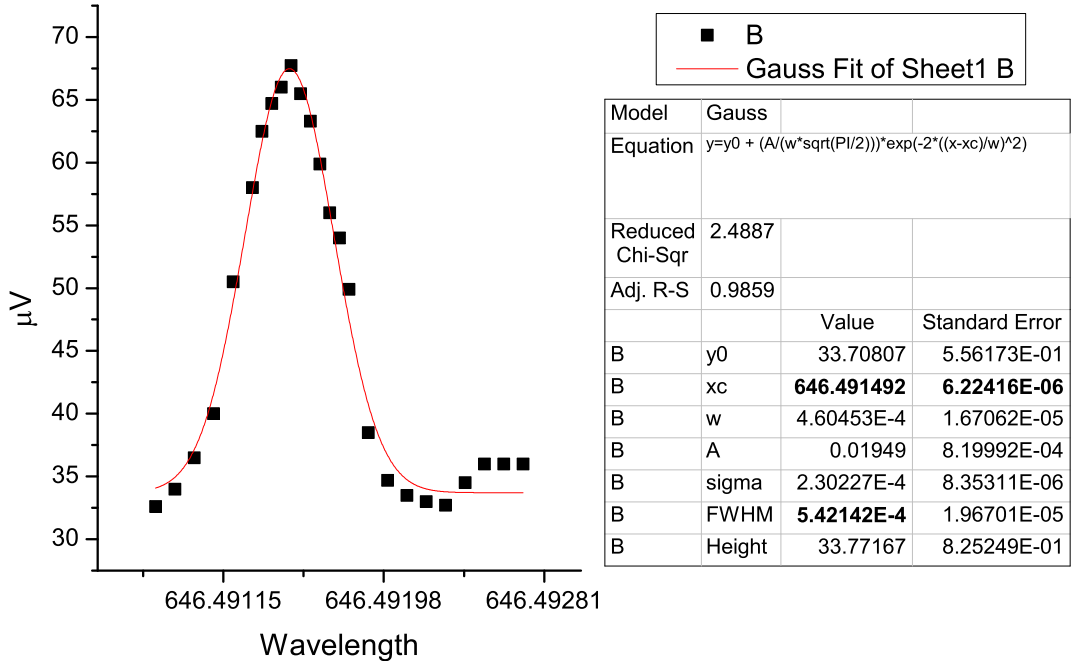

Model	Gauss		
Equation	y=y0 + (A/(w*sqrt(PI/2)))*exp(-2*((x-xc)/w)^2)		
Reduced Chi-Sqr	2.4887		
Adj. R-S	0.9859		
		Value	Standard Error
B	y0	33.70807	5.56173E-01
B	xc	**646.491492**	**6.22416E-06**
B	w	4.60453E-4	1.67062E-05
B	A	0.01949	8.19992E-04
B	sigma	2.30227E-4	8.35311E-06
B	FWHM	**5.42142E-4**	1.96701E-05
B	Height	33.77167	8.25249E-01

FIGURE 4.4: Gaussian Fit of the optogalvanic measurement data of the 646 nm, $F = 7/2$ transition

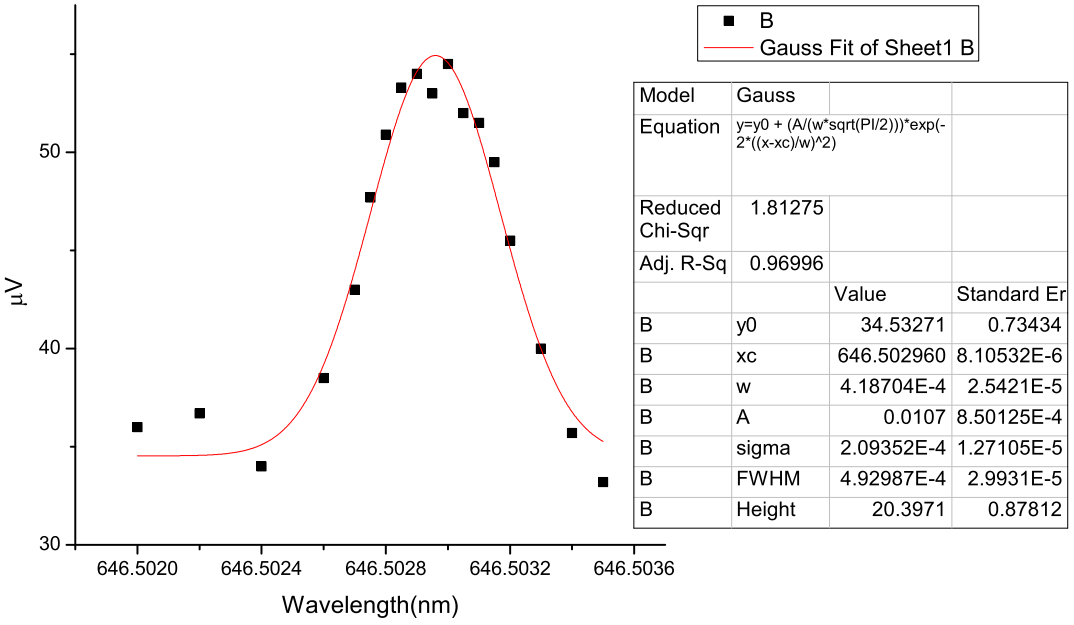

Model	Gauss		
Equation	y=y0 + (A/(w*sqrt(PI/2)))*exp(-2*((x-xc)/w)^2)		
Reduced Chi-Sqr	1.81275		
Adj. R-Sq	0.96996		
		Value	Standard Er
B	y0	34.53271	0.73434
B	xc	646.502960	8.10532E-6
B	w	4.18704E-4	2.5421E-5
B	A	0.0107	8.50125E-4
B	sigma	2.09352E-4	1.27105E-5
B	FWHM	4.92987E-4	2.9931E-5
B	Height	20.3971	0.87812

FIGURE 4.5: Gaussian Fit of the optogalvanic measurement data of the 646 nm, $F = 9/2$ transition

4.1.3 $^1S_0 - {}^3P_1$ Transition at 350 nm

As the 350 nm beam is derived from a 701 nm laser through a frequency doubling cavity, the beam measured by the wavemeter is at 701 nm. The absolute accuracy of the wavemeter is 60 MHz or 0.1 pm at 701 nm, giving equivalent accuracy of 0.05 pm at 350 nm. The wavelength shown in the x-axis of Figure 4.6 is already halved, so the resulting error shown next to it corresponds directly to 350 nm. The wavelength measured in Figure 4.6 corresponds to the transition from

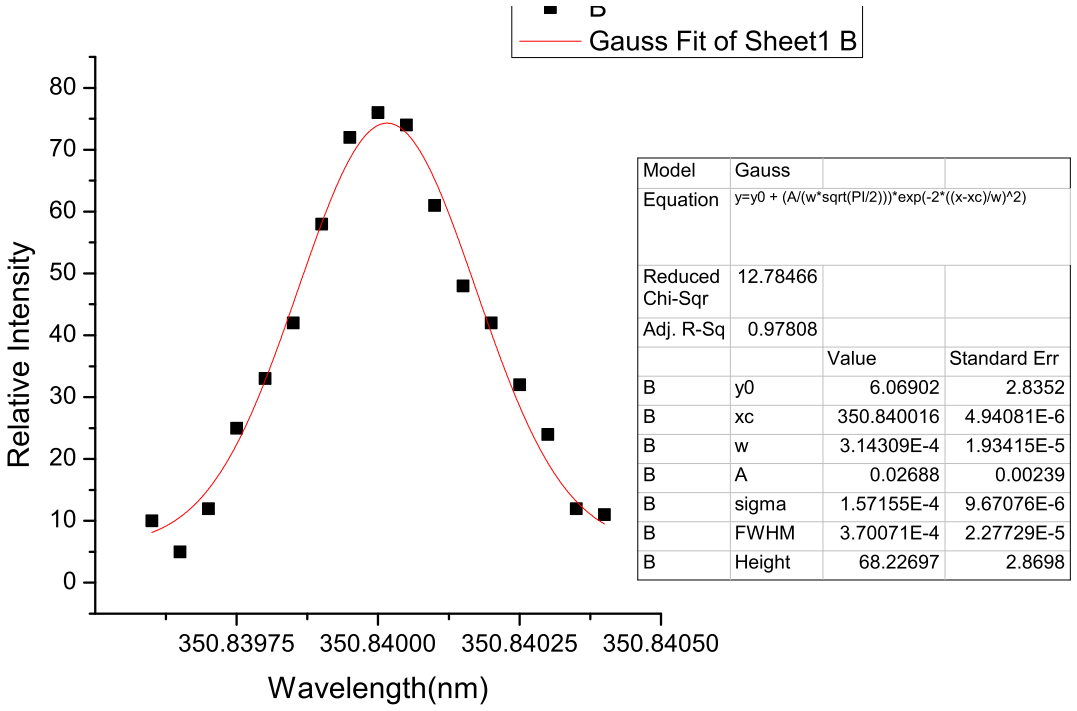

Model	Gauss		
Equation	y=y0 + (A/(w*sqrt(PI/2)))*exp(-2*((x-xc)/w)^2)		
Reduced Chi-Sqr	12.78466		
Adj. R-Sq	0.97808		
		Value	Standard Err
B	y0	6.06902	2.8352
B	xc	350.840016	4.94081E-6
B	w	3.14309E-4	1.93415E-5
B	A	0.02688	0.00239
B	sigma	1.57155E-4	9.67076E-6
B	FWHM	3.70071E-4	2.27729E-5
B	Height	68.22697	2.8698

FIGURE 4.6: Gaussian Fit of the LIF measurement data of the 350 nm transition

ground state to the F=7/2 hyperfine splitting of the $^3P_1$ level. The transitions to F=5/2 and F=9/2 can be calculated using Equation 4.1 and the values of A and B hyperfine coefficients reported by Hartogg *et al.* [30] ($A = +0.166 \pm 0.002\,\mathrm{cm}^{-1}$ and $B = -0.060 \pm 0.003\,\mathrm{cm}^{-1}$). Properly accounting for error propagation, the wavelengths data are summarized as follows:

$$
\begin{aligned}
F = 9/2 \;&\rightarrow\; \lambda = 350.6315 \pm 0.0001\,\mathrm{nm},\;\; \Delta\nu = +20.7 \pm 0.03\,\mathrm{GHz} \\
F = 7/2 \;&\rightarrow\; \lambda = 350.64002 \pm 0.00008\,\mathrm{nm},\;\; \Delta\nu = 0\,\mathrm{GHz} \\
F = 5/2 \;&\rightarrow\; \lambda = 350.6481 \pm 0.0001\,\mathrm{nm},\;\; \Delta\nu = -19.7 \pm 0.02\,\mathrm{GHz}
\end{aligned}
$$

The $\Delta\nu$ values quoted above are the hyperfine separations with respect to the F=7/2 hyperfine level.

4.2 Lifetime Measurement of $^3P_0$ State

This section details the measurement of the characteristic lifetime of the $^3P_0$ level before decaying to either $^3D_1$ or $^3D_2$ via hyperfine mixing while the 646 nm transition is continuously driven. Using the cyclic transition at 646 nm for state detection, the ion will continue fluorescing as long as it stays on the $^3P_0$ level and turn dark otherwise. For the rest of this section, we would refer to these states as bright state and dark state.

The standard 3-step approach to measure this lifetime is the following. First, prepare the ion in the bright state by keeping both 350 nm and 646 nm lasers and 622 LED on. Second, switch off the 350 nm laser and 622 LED simultaneously and record the time taken for it to go dark. Third, repeat this measurement many times. One could then make a histogram that records the number of [decay] occurrences for a given time period. The occurrences are distributed exponentially with parameter τ, the characteristic lifetime of interest.

This technique however is not feasible for our purpose as the lutetium ion is not constantly fluorescing even with all the relevant lasers on. This results from the fact that the 622 LED does not provide adequate repumping out of the $^3D_2$ level (cf. Section 3.4). Shown in Figure 4.7 is a 3000 points sample of the typical blinking signal we obtain, showing higher counts when the ion is in the bright state.

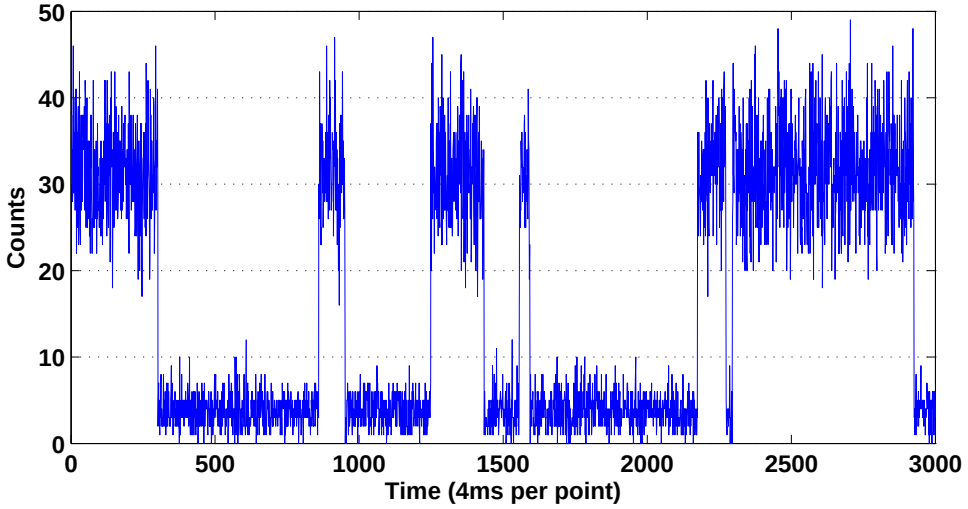

FIGURE 4.7: Raw signal from the counter module at 4 ms binning period.

Due to time constraint, the construction of an additional laser system at 622 nm was not deemed viable. Instead, we decided to perform the lifetime measurement by directly measuring the pulse width of the signal shown in Figure 4.7 and bin them in a histogram. As such, the pulse width of the bright states (bright times) will carry the information on how long does the ion stay bright and the opposite (dark times) will tell us how quickly the 622 LED pump it back to the bright state.

It is important to visually verify the raw signal that there is no indication that the ions swap places during the experiment. The anomaly causes by this can be seen in Figure 4.8 below:

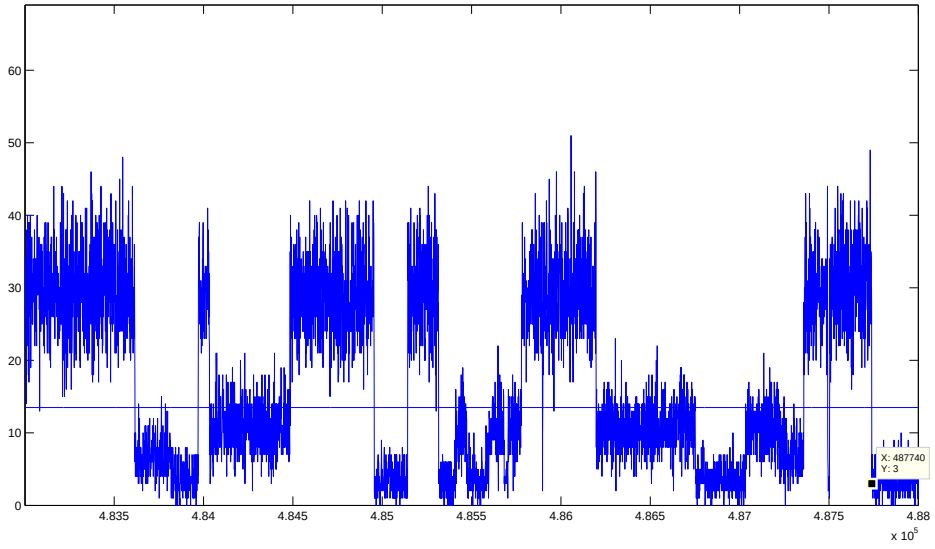

FIGURE 4.8: Part of the raw signal indicating that the ions have swapped places.

4.2.1 Bimodal Poissonian Model

In order to measure the bright times and the dark times, we need to first be able to determine for each point whether it is considered bright or dark. The simplest approach would be to come out with a threshold value by fitting the raw data to a bimodal Poissonian distribution where the two parameters ($\bar{n}_b$ and $\bar{n}_d$) correspond to the average counts rate for the bright state and dark state

respectively.

$$P(n) = p \times \frac{\bar{n}_b^n e^{-\bar{n}_b}}{n!} + (1-p) \times \frac{\bar{n}_d^n e^{-\bar{n}_d}}{n!}. \tag{4.2}$$

The threshold value is then determined by choosing a value that *cuts* out the two modes and minimizes the tails-overlap of the two Poissonian distribution.

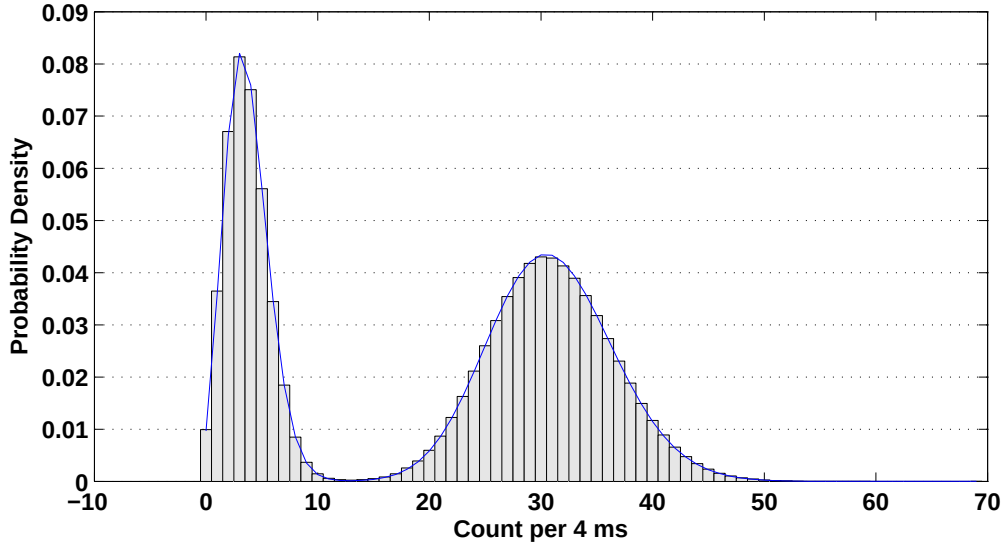

FIGURE 4.9: Bimodal Poissonian fit to raw data.

The estimated parameters corresponding to the fit shown in Figure 4.9 are $\bar{n}_b = 30.975 \pm 0.006\,\text{Cts}/(4\,\text{ms})$, $\bar{n}_d = 3.705 \pm 0.005\,\text{Cts}/(\,4\text{ms})$ and $p = 0.6067 \pm 0.0008$, giving rise to a threshold of $n_0 = 13$. The convention is that a given count value is considered dark if it is $\leq n_0$ and bright otherwise.

Taking the tails-overlap as our error under this Bimodal-Poissonian model, we obtain a detection efficiency of $\eta = 99.987\%$ or equivalently an error of 0.0001325. This error value is a p-weighted average of the tail of the dark poisson distribution that falls above the threshold (false-bright = 0.0000342) and the tail of the bright distribution that falls below the threshold (false-dark = 0.0002282). Even though these errors seem small, it becomes clear later on how they cause serious problem in the bright-times and dark-times histograms.

Take the false-dark case for example, these are points misscounted as dark when they are actually bright, thus they will manifest as anomalous narrow dips (mostly of width one or two). Multiplying the false-dark error with the number of bright data points (~ 773000), we get the total number of 177 narrow dips. This means, the error contributes to 177 additional entries to the first few bins of the

dark times histogram (depending on the bin size), this is huge as the total entries to the histogram itself is only about 2400.

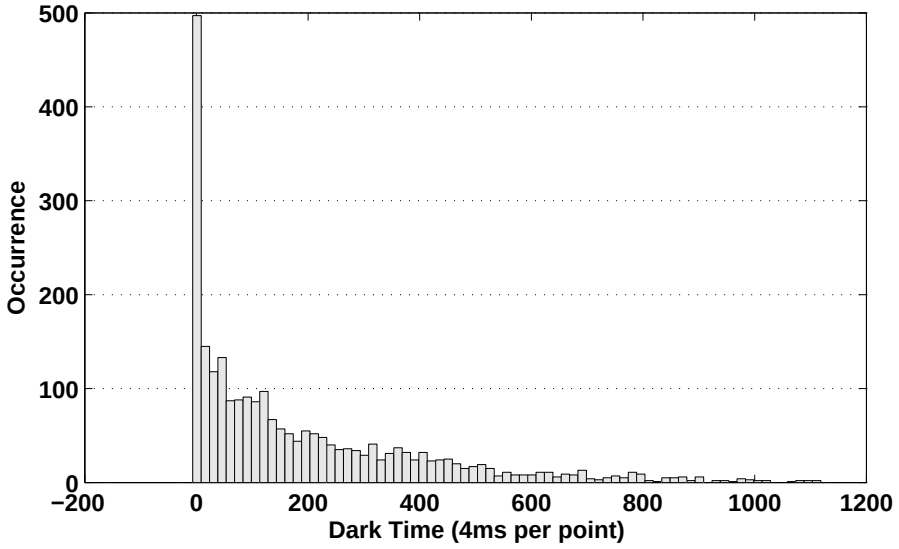

FIGURE 4.10: Effect of the false-dark error to the dark times histogram

This effect is seen clearly in figure Figure 4.10 where the first bin is anomalously overpopulated (the binsize for this is 15). Similar effect on the bright time histogram is also observed. This time it is caused by the false-bright error (anomalous spikes).

One way to treat this problem is by simply trimming the first few bins as the chance of having multiple false-brights consecutively is pretty remote. The trimming process here is equivalent to the process of *state preparation* in the standard procedure, that is to say, a measurement will only be performed when we are sure that the ion is really in the bright state. Unlike a false-bright event, a true bright ion will stay bright for a longer period of time as the rough estimate of the lifetime is $\sim 2\,\mathrm{s}$. The question on how long is long enough is then equivalent to the question of how many bins shall we throw. Section 4.2.2 will provide an answer to this question with the aid of a generalized detection model. The number of bins to be trimmed can be determined by removing them one by one until the exponential parameter value converges and the confidence interval of the estimated parameter reaches a minimum.

The lifetime values obtained from this approach are $\tau_b^\circ = 1249 \pm 25\,\mathrm{ms}$ for the bright time (by removing spikes of width ≤ 2) and $\tau_d^\circ = 935 \pm 20\,\mathrm{ms}$ for the

dark time (by removing dips of width ≤ 10). The parameter estimation was done using maximum likelihood estimator algorithm.

Another subtle effect to account for is the fact that the existence of a dip in the middle of a long bright pulse causes the pulse-width measuring algorithm to count this long bright pulse as two shorter pulses. Evidently, this will affect the bright time histogram and affect the decay rate measured. Fortunately, as this error is also a Poisson process, the inter-arrival time of the error points will follow exponential distribution, just like the decay/repumping processes themselves. As such, the measured rate is simply the actual rate plus the error rate. It is then possible to compensate for this effect if we know the error rate. The error rates are obtained using a generalized detection model elaborated in Section 4.2.2.

4.2.2 Generalized Detection Model

Observation on the significance of these errors has lead us to assess the overlapping area more carefully using a more complex model which also accounts for the possibility of the ion to change state from bright to dark or vice versa during the detection period (the model however, does not account for multiple state changes). Derivation of this model can be found in M. Acton's dissertation [31]. In a given detection window τ_D, the probability of an initially bright ion giving exactly n count is described by:

$$P_b(n) = e^{-\beta_b(\bar{n}_b-\bar{n}_d)}\frac{e^{-\bar{n}_b}\bar{n}_b^n}{n!} + \frac{\beta_b e^{\beta_b\bar{n}_d}}{(1+\beta_b)^{n+1}} \times \{\mathcal{P}(n+1,(1+\beta_b)\bar{n}_b) - \mathcal{P}(n+1,(1+\beta_b)\bar{n}_d)\}, \tag{4.3}$$

and the probability of an initially dark ion giving exactly n count is described by:

$$P_d(n) = e^{-\beta_d(\bar{n}_b-\bar{n}_d)}\frac{e^{-\bar{n}_d}\bar{n}_d^n}{n!} + \frac{\beta_d e^{\beta_d\bar{n}_b}}{(1-\beta_d)^{n+1}} \times \{\mathcal{P}(n+1,(1-\beta_d)\bar{n}_b) - \mathcal{P}(n+1,(1-\beta_d)\bar{n}_d)\}, \tag{4.4}$$

where $\mathcal{P}(n,x) = \frac{1}{(n-1)!}\int_0^x t^{(n-1)}e^{-t}\mathrm{d}t$ is the lower regularized gamma function, n_b and n_d characterize the mean number of photon collected for the bright state and dark state respectively. The lifetimes of the bright state and dark state are embedded in the β parameters i.e. $\beta_b = \frac{\tau_D}{\tau_b(\bar{n}_b-\bar{n}_d)}$ and $\beta_d = \frac{\tau_D}{\tau_d(\bar{n}_b-\bar{n}_d)}$.

Feeding the values of $(p, \bar{n}_b, \bar{n}_d, \tau_b, \tau_d)$ we obtained previously into the generalized model, we can see in Figure 4.11 that this model better accounts for the data near the overlapping zone.

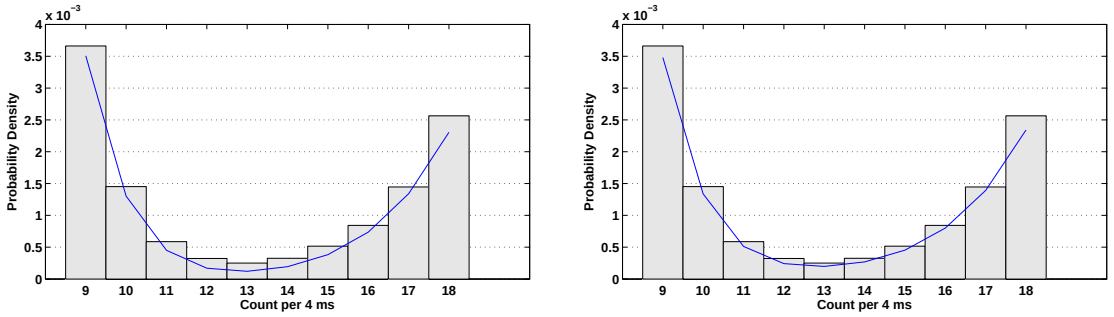

(A) Bimodal Poissonian Model (B) Generalized Detection Model

FIGURE 4.11: Side by side comparison showing how the generalized model better accounts for the data in the overlapping zone.

As the error rate is directly related to the clipped-off tails of the two mode for a given threshold, it is very important to ensure that the model used properly fit the data in this region. Part of the bright distribution that falls below the threshold (bright tail) constitutes a *decay error-rate* (ϵ_b), which affects the measured decay time. On the other hand, part of the dark distribution that falls above the threshold (bright tail) constitutes a *repump error-rate* (ϵ_d), which affects the measured repump time. The following equations detail the calculation of these error rates for a given threshold n_0:

$$\epsilon_b = \frac{1}{\tau_D} \times \sum_{n=0}^{n_0} P_b(n) \tag{4.5}$$

$$\epsilon_d = \frac{1}{\tau_D} \times \sum_{n=(n_0+1)}^{\infty} P_d(n) \tag{4.6}$$

Ideally, one could fit the raw data directly to the generalized detection model and obtain an estimate of the parameters $(p, \bar{n}_b, \bar{n}_d, \tau_b.\tau_d)$, calculate the error rates associated (ϵ_b and ϵ_d), perform error rate correction to τ_b° and τ_d°, and obtain self-consistent results ($\mathcal{T}_b = \tau_b^\circ$ and $\mathcal{T}_d = \tau_d^\circ$). This attempt however, did not work as the estimated τ_b and τ_d from the fit (least-square) are sensitive to the starting points, unlike p, $\bar{n}_b$, and $\bar{n}_d$ which converge to 0.6057, 31.01, and 3.68 respectively regardless of the starting points.

Obtaining p, $\bar{n}_b$, and $\bar{n}_d$ from least-square fit, we could then look for a pair of lifetimes (τ_b, τ_d) that give the most consistent result. In other word, we search for a pair of τ_b and τ_d that minimize $\delta = |\mathcal{T}_b - \tau_b| + |\mathcal{T}_d - \tau_d|$. This approach gives $\tau_b = \mathcal{T}_b = 1849\,\text{ms}$ and $\tau_d = \mathcal{T}_d = 1528\,\text{ms}$ with $\delta = 0.27$ and fit residual $r = 1.86 \times 10^{-6}$. The error rates associated are $\epsilon_b = 2.597 \times 10^{-4}$ and $\epsilon_d = 4.151 \times 10^{-4}$. Without accounting for the uncertainty of the error rates, we quote the following results:

$$\mathcal{T}_b = 1849 \pm 25\,\text{ms},$$
$$\mathcal{T}_d = 1528 \pm 20\,\text{ms},$$

To reaffirm the consistency of this results, we perform the same analysis with the raw data binned every 8 ms instead of 4 ms, yielding the following results which are in agreement with the previous analysis:

$$\mathcal{T}_b = 1854 \pm 25\,\text{ms},$$
$$\mathcal{T}_d = 1568 \pm 20\,\text{ms},$$

with uncorrected rates of $\tau_b^\circ = 1383$ and $\tau_d^\circ = 946$, error rates of $\epsilon_b = 1.837 \times 10^{-4}$ and $\epsilon_d = 4.196 \times 10^{-4}$. The p, $\bar{n}_b$, and $\bar{n}_d$ parameters converge to 0.6089, 62.01, and 7.38 respectively with a residual of $r = 2.67 \times 10^{-6}$. The inconsistency parameter is $\delta = |\mathcal{T}_b - \tau_b| + |\mathcal{T}_d - \tau_d| = 0.75$.

Figure 4.12 shows how the generalized detection model better accounts for the data near the overlapping zone (threshold $n_0 = 25$).

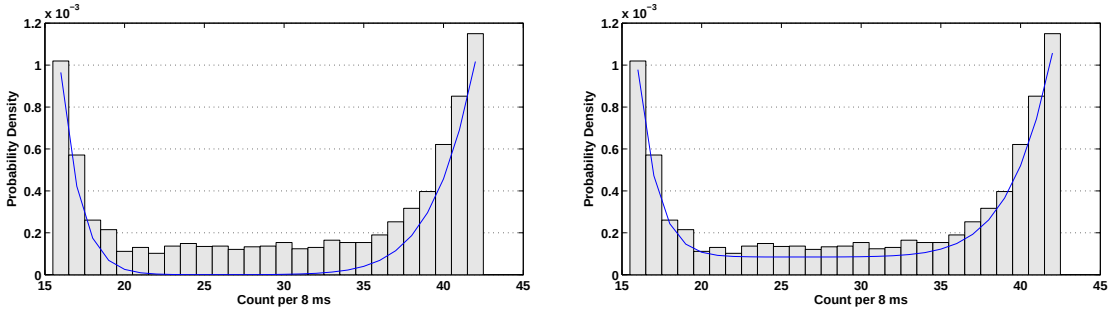

(A) Bimodal Poissonian Model (B) Generalized Detection Model

FIGURE 4.12: Comparison between the generalized detection model (right) and the standard bimodal-Poissonian model (left).

Further treatment is required to quantify the uncertainties associated to the error rates, which depend on how well the model represents the data. This proved to be challenging as we did not manage to run any *goodness of fit* test with the generalized model, not even least-square fitting nor maximum likelihood parameter estimates as the model is rather complex.

One approach to quantify the uncertainty of the error rate is to numerically evaluate its upper bound (when $\bar{n}_b = 31.01 - 0.006$ and $\bar{n}_d = 3.68 + 0.005$) and lower bound (when $\bar{n}_b = 31.01 + 0.006$ and $\bar{n}_d = 3.68 - 0.005$). Calculated this way, we found that the uncertainties are in the order of 10^{-7}. Following the error propagation rule, this error will be added up together with the $\tau^{-2}\delta\tau$ term which is in the order of 10^{-5}. As such, it is safe to ignore the uncertainty of the error rate.

Thus far we have not addressed the issue of state preparation i.e. the ideal number of bins to remove (cf. Section 4.2.1). Referring to Equation 4.3 and Equation 4.4, we see that P_b and P_d both consist of two terms. The first one correspond to the case of no change in state during detection and the second term corresponds to the case where the ion changes state during detection. We could then treat each of these terms separately as follows:

Take the probability of a bright ion giving n count ($P_b(n)$) for example, summing it up from 0 to n_0 (threshold) gives the probability of a bright ion detected as dark. Considering the two terms in the expression separately, we have:

$$P_{bdb} = \sum_{n=0}^{n_0} e^{-\beta_b(\bar{n}_b - \bar{n}_d)} \frac{e^{-\bar{n}_b}\bar{n}_b^n}{n!}, \tag{4.7}$$

$$P_{bdd} = \sum_{n=0}^{n_0} P_b(n) - P_{bdb}, \tag{4.8}$$

where P_{bdb} is the probability of a bright ion (b) detected as dark (d) and stays bright (b), hence the notation (bdb). Similarly for the summation of the second term, P_{bdd} is the probability of a bright ion detected as dark and turns dark. By the same token, one can calculate P_{bbb} by summing the first term of $P_b(n)$ from $n_0 + 1$ to ∞, or P_{dbd} by summing the second term of $P_d(n)$ from $n_0 + 1$ to ∞.

Having this established, we can then calculate the probability of having anomalous spikes/dips of width 1, 2, ... ℓ. Take for example a dip of width one, three consecutive data points whereby the first one is detected as bright, second

one dark and third one bright again. As we are considering an anomalous dip i.e. a dip recorded when there is no actual transition going on, the actual state of the ion is bright, bright and bright for all three data points. The probability of having such an event is then simply described by $P_{dip-1} = P_{bbb} \times P_{bdb} \times P_{bbb}$.

Extending this reasoning for the case of an anomalous dip of length l, we have $P_{dip-\ell} = P_{bbb} \times (P_{bdb})^{\ell} \times P_{bbb}$. We can then decide on the number of bins to remove by simply looking for the smallest value of ℓ that gives a reasonably small number of anomalous histogram entries.

For our calculation of τ_b, we have chosen to remove spikes of width two or less. We can now check whether this is reasonable by calculating the following:

$$P_{spike-1} = P_{ddd}(P_{dbd})^1 P_{ddd} = 1.3 \times 10^{-4} \tag{4.9}$$

$$P_{spike-2} = P_{ddd}(P_{dbd})^2 P_{ddd} = 1.7 \times 10^{-8} \tag{4.10}$$

$$P_{spike-3} = P_{ddd}(P_{dbd})^3 P_{ddd} = 2.3 \times 10^{-12} \tag{4.11}$$

Multiplying these probabilities with the total number of data points in the dark distribution (~ 502000), we have ~ 65 anomalous entries of width 1, ~ 0.01 anomalous entries of width 2 and $\sim 10^{-6}$ anomalous entries of width 3. So by getting rid of all entries of width 1 and 2 and re-bin our histogram, we are sure that our τ_b measurement is no longer affected by this effect. Figure 4.13 shows a histogram fit with these entries removed.

Similar calculation was done for the measurement of τ_d, verifying that removing entries of width less than 11 is the right choice. Unlike τ_b, the value of τ_d merely tells us about the repumping efficiency of the 622nm LED and has nothing to do with the lifetimes of any energy level.

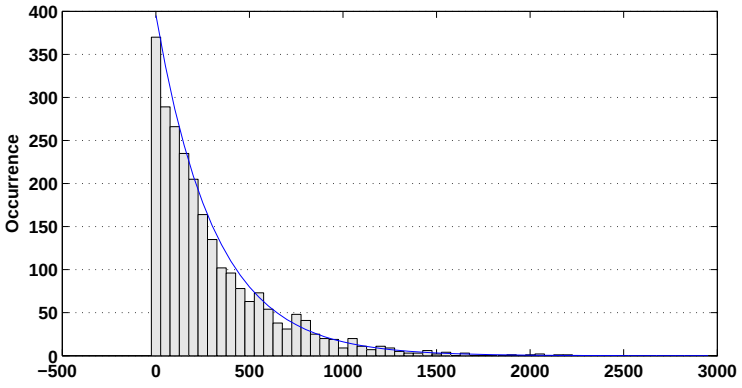

FIGURE 4.13: Histogram of bright-times with an exponential fit curve

4.3 Future Work

The next step for this project would be to look for the clock transition at 848 nm ($^1S_0 - {}^3D_1$) and to perform some characterization measurements. As the natural linewidth of this transition is very narrow ($\sim$ nHz), a stable reference and a narrow linewidth laser system at 848 nm need to be assembled. In addition, another optogalvanic spectroscopy may need to be performed on the 598 nm transition ($^3P_1 - {}^3D_1$) in order to obtain more precise wavelength information on the clock transition.

Chapter 5

Conclusion

Optogalvanic spectroscopy and Laser Induced Fluorescence (LIF) spectroscopy have allowed us to obtain preliminary transition wavelength data associated to the energy levels relevant to atomic clock application. Results obtained in this project support the proposition of using Lu II as an single-ion based clock candidate. The $^3P_0 - {}^3D_1$ cyclic transition has been successfully driven at 646 nm with the aid of repump beams at 350 nm laser and 622 nm. We believe that a steady fluorescence could be achieved by replacing the 622 LED with a laser system to provide adequate repumping. The forbidden transition from $^3P_0$ level to $^1S_0$ or $^3D_1$ was measured to have a lifetime of 1.849 s, long enough for the cyclic transition to be used as a means of state detection. Doppler cooling of Lu II on the 646 nm transition will be attempted in the future once a steady fluorescence is achieved. Optimal Doppler cooling could be achieved by optimizing the detuning of the sidebands of the 646 nm laser with respect to the hyperfine splittings of the $^3D_1$ level. More precise value of the 848 nm clock transition can be deduced from the optogalvanic spectroscopy measurements of the 350 nm transition which has been performed and the 598 nm transition which is yet to be performed.

Appendix A

Pictures of Experimental Setup

A.1 Optogalvanic Setup

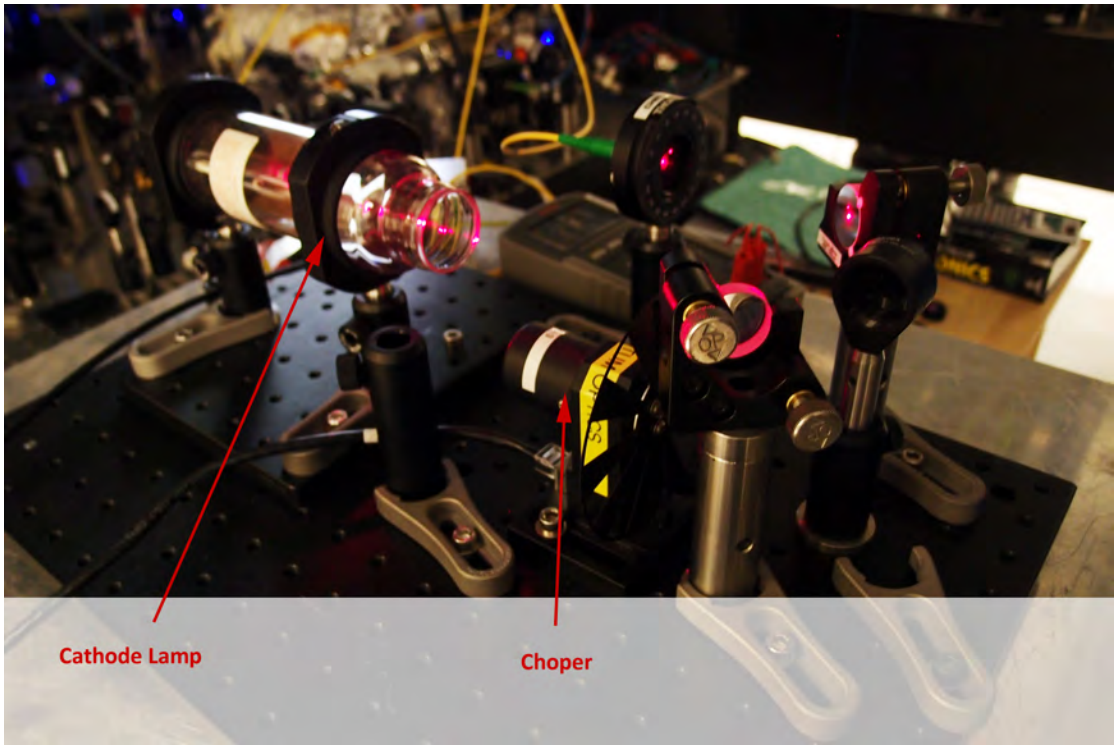

FIGURE A.1: Picture of the actual Optogalvanic Setup

A.2 LIF Setup

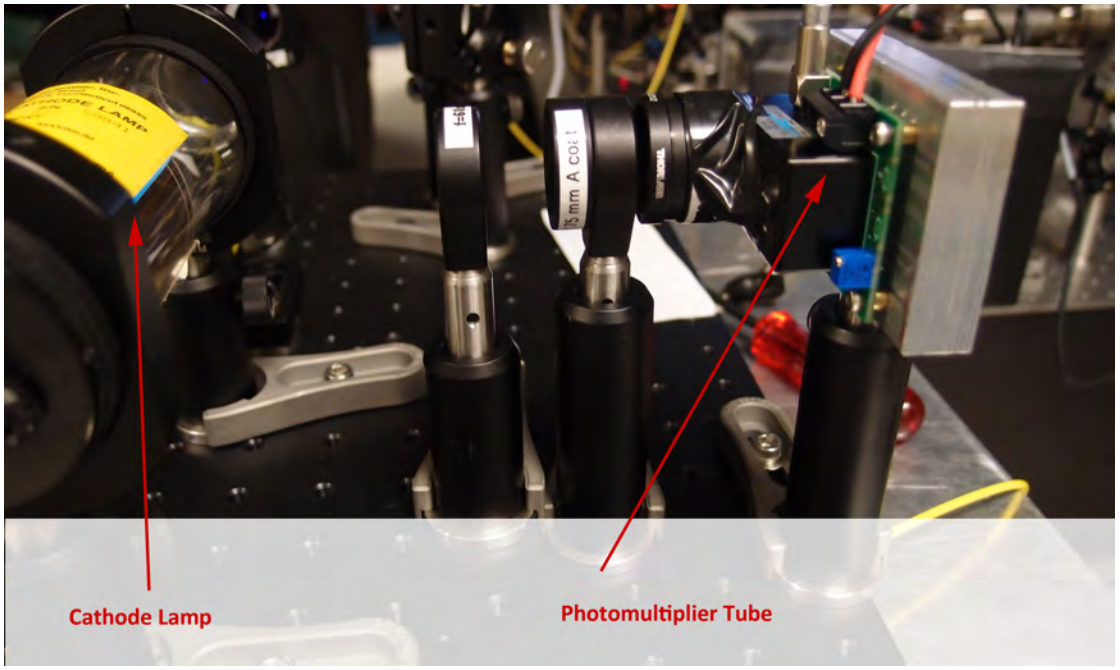

FIGURE A.2: Picture of the actual LIF Setup

A.3 Imaging System

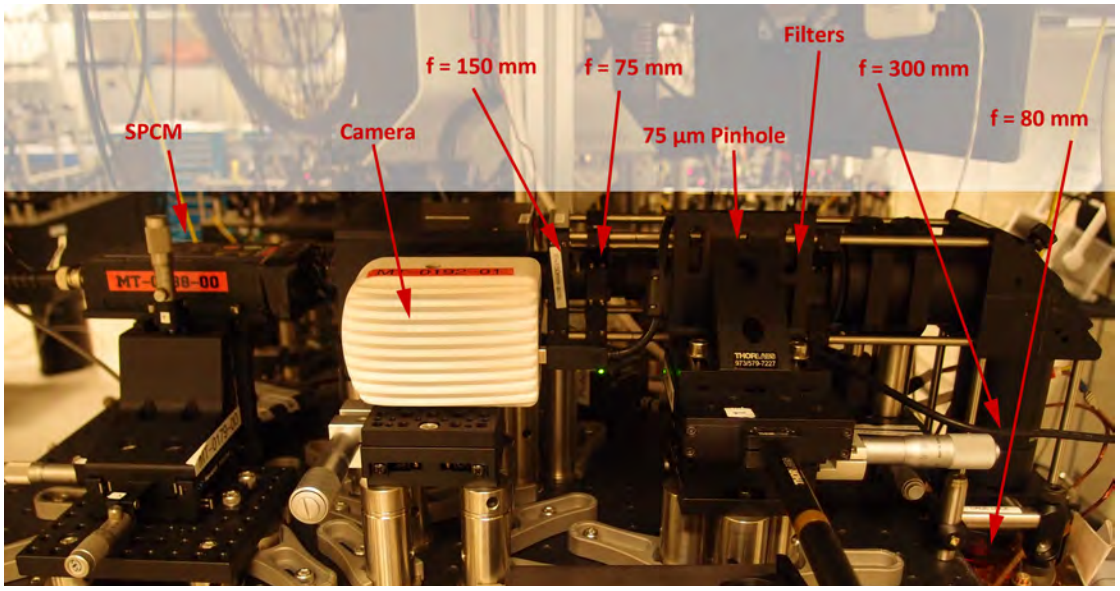

FIGURE A.3: Picture of the actual imaging system

A.4 646 nm Laser System

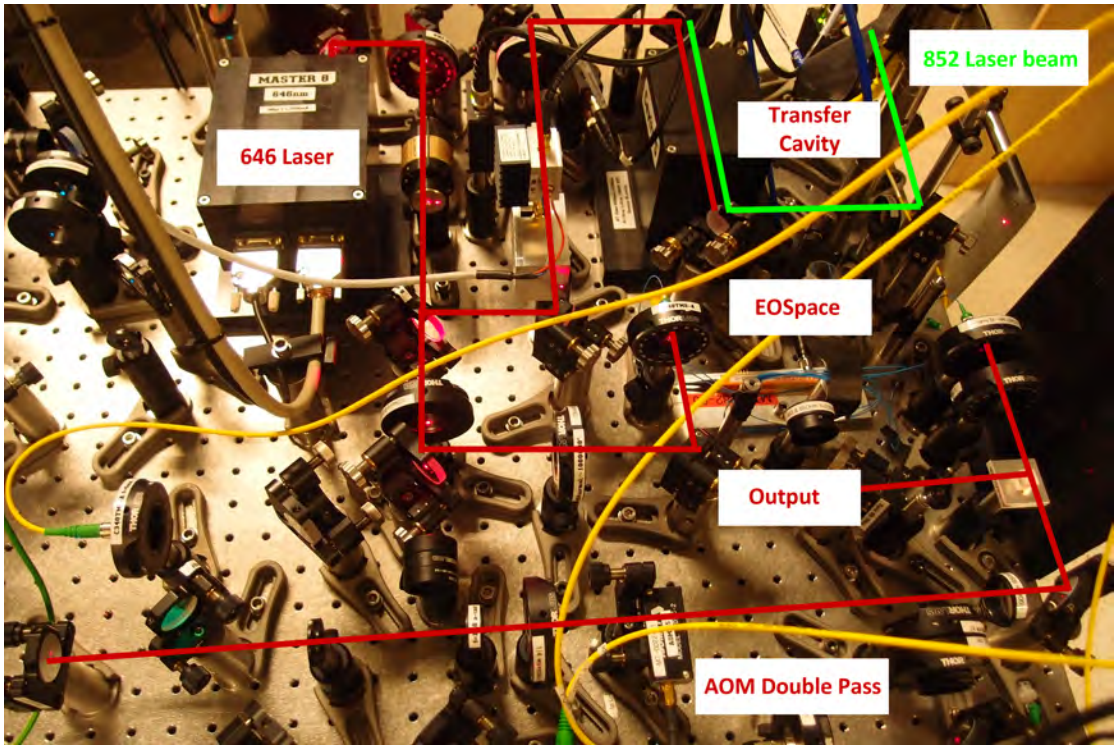

FIGURE A.4: Picture of the actual 646 nm laser system

A.5 350 nm Laser System

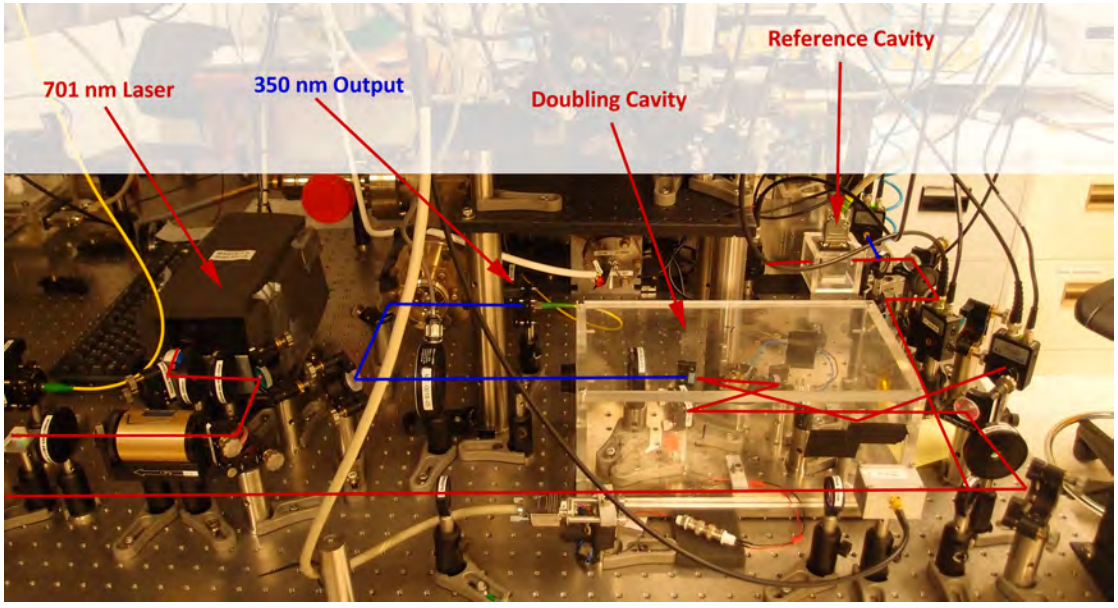

FIGURE A.5: Picture of the actual 350 nm laser system

A.6 Ion Trap

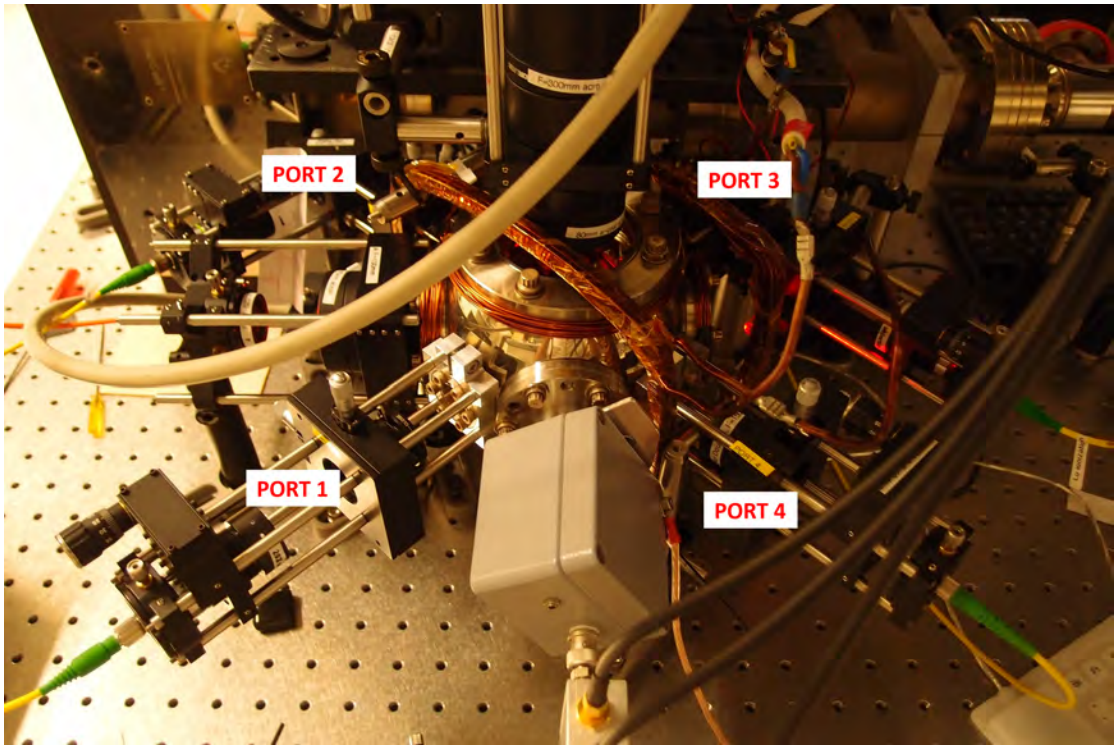

FIGURE A.6: Picture of the actual ion trap

Bibliography

[1] J. A. Fedchak, E. A. Den Hartog, and J. E. Lawler. Experimental and theoretical radiative lifetimes, branching fractions, and oscillator strengths for lu i and experimental lifetimes for lu ii and lu iii. *The Astrophysical Journal*, 542(2):1109–1118, 2000.

[2] P. Quinet, P. Palmeri, E. Biemont, M. M. McCurdy, G. Rieger, E. H. Pinnington, M. E. Wickliffe, and J. E. Lawler. Experimental and theoretical radiative lifetimes, branching fractions and oscillator strengths in lu ii. *Monthly Notices of the Royal Astronomical Society*, 307(4):934–940, 1999. ISSN 1365-2966.

[3] W. F. Meggers, C. H. Corliss, and B. F. Scribner. Tables of spectral line intensities, part i arranged by elements, part ii arranged by wavelengths. *Natl. Bur. Stand. Monograph*, 145(2):600pp, 1975.

[4] J. Sugar and C.H. Corliss. *Atomic energy levels of the iron-period elements, potassium through nickel*. SUPPLEMENT 2 VOLUME 14. Published by the American Chemical Society and the American Institute of Physics for the National Bureau of Standards, 1985. ISBN 9780883184806.

[5] J. E. Sansonetti and G. Nave. Wavelengths, transition probabilities, and energy levels for the spectrum of neutral strontium (sri). *Journal of Physical and Chemical Reference Data*, 39(3):033103, 2010.

[6] A E Nilsson, S Johansson, and R L Kurucz. The spectrum of singly ionized yttrium, y ii. *Physica Scripta*, 44(3):226, 1991.

[7] L. Essen and J. V. L. Parry. An Atomic Standard of Frequency and Time Interval: A Cæsium Resonator. *Nature*, 176:280–282, August 1955. doi: 10.1038/176280a0.

[8] T. Rosenband, D. B. Hume, P. O. Schmidt, C. W. Chou, A. Brusch, L. Lorini, W. H. Oskay, R. E. Drullinger, T. M. Fortier, J. E. Stalnaker, S. A. Diddams, W. C. Swann, N. R. Newbury, W. M. Itano, D. J. Wineland, and J. C. Bergquist. Frequency ratio of al+ and hg+ single-ion optical clocks; metrology at the 17th decimal place. *Science*, 319(5871):1808–1812, 2008. doi: 10.1126/science.1154622.

[9] H. Katori M. Takamoto, T. Takano. Frequency comparison of optical lattice clocks beyond the Dick limit. *Nature Photonics*, 5:288–292, April 2011. doi: 10.1038/nphoton.2011.34.

[10] A. D. Ludlow, T. Zelevinsky, G. K. Campbell, S. Blatt, M. M. Boyd, M. H. G. de Miranda, M. J. Martin, J. W. Thomsen, S. M. Foreman, Jun Ye, J. E. Fortier, T. M.and Stalnaker, S. A. Diddams, Z. W. Le Coq, Y.and Barber, N. Poli, N. D. Lemke, K. M. Beck, and C. W. Oates. Sr lattice clock at 1×10^{-16} fractional uncertainty by remote optical evaluation with a ca clock. *Science*, 319(5871):1805pp, 2008. doi: 10.1126/science.1154622.

[11] N. Hinkley, J. A. Sherman, N. B. Phillips, M. Schioppo, N. D. Lemke, K. Beloy, M. Pizzocaro, C. W. Oates, and A. D. Ludlow. An atomic clock with 10^{-18} instability. *Science*, 341(6151):1215–1218, 2013. doi: 10.1126/science.1240420.

[12] C.-Y. Xu, S.-M. Hu, J. Singh, K. Bailey, Z.-T. Lu, P. Mueller, T. P. O'Connor, and U. Welp. Optical excitation and decay dynamics of ytterbium atoms embedded in a solid neon matrix. *Phys. Rev. Lett.*, 107: 093001, Aug 2011. doi: 10.1103/PhysRevLett.107.093001.

[13] V. I. Yudin, A. V. Taichenachev, M. V. Okhapkin, S. N. Bagayev, Chr. Tamm, E. Peik, N. Huntemann, T. E. Mehlst aubler, and F. Riehle. Atomic clocks with suppressed blackbody radiation shift. *Phys. Rev. Lett.*, 107: 030801, Jul 2011. doi: 10.1103/PhysRevLett.107.030801.

[14] Chang Guoqing. Trapping lutetium ions. Master's thesis, National University of Singapore, 2013.

[15] J. E. Lawler, A. I. Ferguson, J. E. M. Goldsmith, D. J. Jackson, and A. L. Schawlow. Doppler-free intermodulated optogalvanic spectroscopy. *Phys. Rev. Lett.*, 42:1046–1049, Apr 1979. doi: 10.1103/PhysRevLett.42.1046.

[16] W. Demtröder. *Laser Spectroscopy: Basic Concepts and Instrumentation*. Springer, 2002.

[17] D. J. Berkeland, J. D. Miller, J. C. Bergquist, W. M. Itano, and D. J. Wineland. Minimization of ion micromotion in a paul trap. *Journal of Applied Physics*, 83(10), 1998.

[18] Kristian Mølhave. Constructions of and experiments with a linear paul trap. Master's thesis, University of Aarhus, 2000.

[19] W. M. Itano D. Leibfried B.E. King D. J. Wineland, C. Monroe and D.M. Meekhof. Experimental issues in coherent quantum-state manipulation of trapped atomic ions. *Journal of Applied Physics*, 103(3), 1998.

[20] Wayne M Itano, J C Bergquist, J J Bollinger, and D J Wineland. Cooling methods in ion traps. *Physica Scripta*, 1995(T59):106, 1995.

[21] A. Steane. The ion trap quantum information processor. *Appl Phys. B*, 64: 623–642, 1997.

[22] Christopher J. Foot. *Atomic Physics*. Oxford University Press, 2005.

[23] Ferdinand Schmidt-Kaler, Jürgen Eschner, Rainer Blatt, Dietrich Leibfried, Christian Roos, and Giovanna Morigi. Laser cooling of trapped ions. In Hartmut Figger, Claus Zimmermann, and Dieter Meschede, editors, *Laser Physics at the Limits*, pages 243–260. Springer Berlin Heidelberg, 2002. ISBN 978-3-642-07627-5.

[24] D. S. Goodman, I. Sivarajah, J. E. Wells, F. A. Narducci, and W. W. Smith. Ion neutral atom sympathetic cooling in a hybrid linear rf paul and magneto optical trap. *Phys. Rev. A*, 86:033408, Sep 2012.

[25] R. de Carvalho et al. Electronic structure calculations. *Eur. Phys. J. D7*, pages 289–309, 1999.

[26] D. J. Larson, J. C. Bergquist, J. J. Bollinger, Wayne M. Itano, and D. J. Wineland. Sympathetic cooling of trapped ions: A laser-cooled two-species nonneutral ion plasma. *Phys. Rev. Lett.*, 57:70–73, Jul 1986.

[27] M. G. Raizen, J. M. Gilligan, J. C. Bergquist, W. M. Itano, and D. J. Wineland. Ionic crystals in a linear paul trap. *Phys. Rev. A*, 45:6493–6501, May 1992.

[28] D. J. Wineland, J. C. Bergquist, Wayne M. Itano, J. J. Bollinger, and C. H. Manney. Atomic-ion coulomb clusters in an ion trap. *Phys. Rev. Lett.*, 59: 2935–2938, Dec 1987.

[29] H Maeda, Y Mizugai, Y Matsumoto, A Suzuki, and A Takami. Highly excited even rydberg series of lu i studied by two-step laser photoionisation spectroscopy. *Journal of Physics B: Atomic, Molecular and Optical Physics*, 22(18):L511, 1989.

[30] E.A. Den Hartog, J.J. Curry, M.E. Wickliffe, and J.E. Lawler. Spectroscopic data for the 6s6p $^3p_1$ level of lu+ for the determination of the solar lutetium abundance. *Solar Physics*, 178(2):239–244, 1998. ISSN 0038-0938. doi: 10.1023/A:1005088315480.

[31] M. Acton. *Detection and Control of Individual Trapped Ions and Neutral Atoms*. PhD thesis, University of Michigan, 2008.